Discoveries in Phononic Crystals and Acoustic Metamaterials

Discoveries in Phononic Crystals and Acoustic Metamaterials

A DISSERTATION PRESENTED
BY
PAI WANG
TO
THE SCHOOL OF ENGINEERING AND APPLIED SCIENCES

IN PARTIAL FULFILLMENT OF THE REQUIREMENTS
FOR THE DEGREE OF
DOCTOR OF PHILOSOPHY
IN THE SUBJECT OF
APPLIED MATHEMATICS

HARVARD UNIVERSITY
CAMBRIDGE, MASSACHUSETTS
SEPTEMBER 2015

Thesis advisor: Professor Katia Bertoldi Pai Wang

Discoveries in Phononic Crystals and Acoustic Metamaterials

Abstract

Phononic crystals and acoustic metamaterials are heterogeneous materials that enable manipulation of elastic waves. An important characteristic of these heterogeneous systems is their ability to tailor the propagation of elastic waves due to the existence of band gaps – frequency ranges of strong wave attenuation. In this Thesis, I report discoveries of three new types of band gaps: i) Band gaps induced by geometric frustration in periodic acoustic channel networks; ii) Band gap induced by high connectivity in periodic beam lattices; and iii) Topological band gaps in gyroscopic phononic crystals that protects one-way edge waves. The investigations presented here shed new light on the rich dynamic properties of phononic crystals and acoustic metamaterials, opening avenues for new strategies to control mechanical waves in elastic systems.

Contents

List of Figures

Acknowledgments

I would like to first express my deep gratitude towards my advisor, Prof. Katia Bertoldi. As a mentor, she is motivating, supportive, and patient with students; as a group leader, she is knowledgeable, confident and persistent on pursuits. All my research projects are made possible with her continuous guidance and repeated encouragements.

I am deeply in debt to my colleagues and friends in the graduate school, especially Sicong Shan, Prof. Sung Hoon Kang, Prof. Jongmin Shim, Dr. Filippo Casadei, Dr. Farhad Javid, Sahab Babaee, Jia Liu, Johannes Overvelde, Qihan Liu and Jianyu Li, who offered tremendous help during my study here.

I highly appreciate the graduate courses and lectures I attended at Harvard, especially those instructed by Prof. Zhigang Suo, Prof. Joost Vlassak, Dr. David Knezevic, Prof. John Hutchinson, Prof. James Rice, Prof. Ariel Amir and Prof. Michael Brenner. The intellectual interactions with these great minds have been one of the most fun and inspiring experiences I had in my life.

I am especially grateful to Prof. Joost Vlassak and Prof. David Clarke, who have generously offered their laboratories for my experiments.

I would also like to thank all my collaborators Dr. James Weaver, Cangyu Qu, Dr. Samuel Shian,

Dr. Elizabeth Chen, Dr. Jordan Raney, Lichen Fang, Francisco Candido, Yushen Sun, Joyce Zhu, Xiuming Zhang, Sijie Sun, Yue Zheng, Kai Xu, Matheus Fernandes, Dr. Fatih Goncu, Dr. Patrick Kurzeja and Dr. Ling Lu. I have benefited substantially from the discussions and exchange of ideas with them.

My graduate study would not have been possible without the devoted love and understanding from my parents. I would like to give my special thanks to my wife Jing Ma, whose unconditional love, deep care and constant supports enabled me to finish my thesis.

To achieve great things, two things are needed; a plan, and not quite enough time.

Leonard Bernstein

1 Introduction

Artificially structured composite materials that enable manipulation of elastic waves have received significant interest in recent years, not only because of their rich physics, but also for their broad range of applications[71,46]. An important characteristic of these heterogeneous systems is their ability to tailor the propagation of elastic waves due to the existence of band gaps – frequency ranges of strong wave attenuation.

In phononic crystals, band gaps are generated by Bragg scattering – the scattering of waves by a

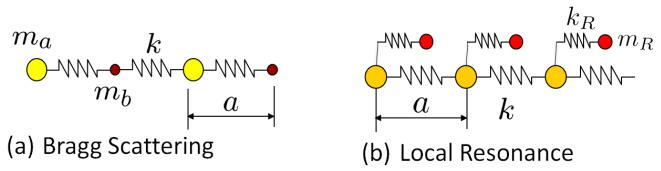

Figure 1.1: Two types of mechanisms to form band gaps in elastic system (a) 1D discrete model for phononic crystals; and (b) 1D discrete model for locally resonant acoustic metamaterials.

periodic arrangement of scatterers with dimensions and periods comparable to the characteristic wavelengths (a simple discrete example system in 1D is shown in Fig. 1.1a). In contrast, for acoustic metamaterials, localized resonance within the medium is exploited to attenuate the propagation of waves. In this case, The local resonant modes are designed to hybridize with the propagating wave modes to produce a range of exotic behaviors, such as band gaps, negative refraction and negative effective dynamic properties (a simple discrete example system 1D is shown in Fig. 1.1b).

Historically, the study of wave propagation in geometrically ordered media can date back to Rayleigh's treatment of wave propagations in geometrically ordered media in his book *The Theory of Sound*[99]. Since then, this research topic has grown significantly into an emerging multi-disciplinary area that encompasses concepts and techniques from both condensed matter physics and acoustical engineering. The technical word, "phonon", originally came from the study of vibrations of atomic crystal lattices. In general condensed matter physics, it is defined as the quantum of vibrational energy and the quasi-particle representing sound in a solid. In recent years, the term also gained popularity in studies on classical waves and acoustics, especially in the context of geometrically ordered media[71,46]. After the discovery of the first complete phononic band gap by Sigalas and Economou[107] in 1993, a new term, "phononic crystal", was then coined by Kushwaha and his colleagues[56], differentiating it from its counterparts in electronics and optics. On the other hand, "acoustic metamaterials" are typically associated with localized resonances, which was first demonstrated in the pioneering work by Liu and his colleagues[68] in 2000, and has since proliferated into a

rich subject with numerous applications.

During the last decade, there has been a fast growing number of research activities in the study of phononic crystals and acoustic metamaterials. Their band gap properties have been exploited to design devices for noise reduction[31,103,77], vibration control[18,13,54] and wave guiding[52,113,88,20], and these practical applications have generated rising interest in the fundamental mechanisms and controlling parameters of band gaps.

In this thesis, numerical simulations and experiments are combined to investigate three new types of band gaps.

First, in Chapter 2, I demonstrate both numerically and experimentally a new type of band gaps induced by geometric frustration in two-dimensional acoustic networks consisting of a periodic array of narrow air channels. Interestingly, while resonant modes are ubiquitous in all network geometries, we show that they give rise to band gaps only in the geometrically frustrated ones (i.e. those comprising triangles and pentagons). Our results not only reveal a new mechanism to control the propagation of waves in specific frequency ranges, but also open avenues for the design of a new generation of smart systems to manipulate sound and vibrations.

Second, Chapter 3 shows that by tuning the average connectivity of a beam network, locally resonant band gaps can also be generated in structures without embedding additional resonating units. In particular, a critical threshold for average connectivity is identified, far from which the band gap size is purely dictated by the global lattice topology. By contrast, near this critical value, the detailed local geometry of the lattice also has strong effects. Moreover, in stark contrast to the static case, we find that the nature of the joints is irrelevant to the dynamic response of the lattices. Our results not only shed new light on the rich dynamic properties of periodic lattices, but also outline a new strategy to manipulate mechanical waves in elastic systems.

Third, Chapter 4 reports a new type of phononic crystals with topologically nontrivial band gaps for both longitudinal and transverse polarizations, resulting in protected one-way elastic edge

waves. In our design, gyroscopic inertial effects are used to break the time-reversal symmetry and realize the phononic analogue of the electronic quantum (anomalous) Hall effect. We investigate the response of both hexagonal and square gyroscopic lattices and observe bulk Chern numbers of 1 and 2, indicating that these structures support single and multi-mode edge elastic waves immune to backscattering. These robust one-way phononic waveguides could potentially lead to the design of a novel class of surface wave devices that are widely used in electronics, telecommunication, and acoustic imaging.

Finally, concluding remarks on all three new types of band gaps and the future outlook of the research field of phononic crystals and acoustic metamaterials are given in Chapter 5.

Any intelligent fool can make things bigger, more complex, and more violent.
It takes a touch of genius—and a lot of courage to move in the opposite direction.

Albert Einstein

2

Band Gap by Geometric Frustration

The content of this chapter will be published in *Wang P, Zheng Y, Fernandes M, Sun Y, Xu K, Sun S, Kang SH, Bertoldi K. Acoustic band gaps induced by geometric frustration. under review.*

Geometric frustration arises when interactions between the degrees of freedom in a lattice are incompatible with the underlying geometry[102,81]. This phenomenon plays an important role in many natural and synthetic systems, including water ice[89], spin ice[42,7,128,97,58,28,83,8,33,147,2], colloids[41,106,144,23,105], liquid crystals[145] and proteins[15,134]. Surprisingly, despite the fact that geometrical frustration is scale-free, it has been primarily studied at the micro-scale[81] and only very recently the rich behavior of macroscopic frustrated systems[79,51], which can be easily fabricated and manipulated, started to get explored.

Here, we investigate the effect of geometric frustration on the propagation of sound waves in macroscopic acoustic networks comprising a lattice of narrow air channels. While an unfrustrated square network transmits acoustic waves of any frequency, we demonstrate both numerically and experimentally that in a triangular network geometric frustration provides a new mechanism to generate sonic band gaps - ranges of frequency in which the waves cannot propagate through the acoustic network. In fact, sonic band gaps have been previously achieved either by the Bragg-type collective scattering and interference in ordered arrays of solid inclusions in air[108,55,73,104,100] or by resonant hybridization and energy localization in channels with embedded resonators[112,139,44,32]. In contrast, our results indicate that, by harnessing geometric frustration, hybridization band gaps can be induced in networks of air channels without the need of embedding additional resonators.

We start by calculating the dispersion relation for acoustic networks comprising a periodic array of narrow air channels of length L and cross-sectional width t, for which $t << L$. In any individual channel the free vibrations of the enclosed air column can be described by the 1D wave equation[84], which can be solved analytically yielding the resonance angular frequencies

$$\omega_n = \frac{n\pi c}{L} = \frac{2\pi c}{\lambda_n}, \qquad n = 1, 2, 3... \tag{2.1}$$

where c is the speed of sound in the channel and we have assumed both ends of the channel to be

either open or closed. Differently, for a periodic network of air channels the wave equation can only be solved numerically because of the complex geometry. In particular, here we use the finite element (FE) method and discretize the acoustic lattice into a number of 1D elements. The dispersion relation for an acoustic network is then calculated by focusing on its unit cell, applying Bloch type boundary conditions, and solving the discretized equation:

$$[\mathbf{K}(\mathbf{k}) - \omega^2 \mathbf{M}]\, \mathbf{p} = 0, \tag{2.2}$$

for wave vectors $\mathbf{k}$ within the first Brillouin zone (more details on the algorithm are provided in Appendix A). Note that in Eq. (2.2) ω denotes the angular frequency of the propagating pressure wave, $\mathbf{p}$ is a vector containing the nodal values of the acoustic pressure and $\mathbf{K}$ and $\mathbf{M}$ are the acoustic stiffness and mass matrices, respectively.

In Fig. 2.1 we show the acoustic dispersion relations in terms of the normalized frequency $\Omega = \omega/\omega_2 = \omega L/(2\pi c)$ calculated for square and triangular acoustic networks. Both band structures are characterized by equally spaced flat bands located at $\Omega = n/2$ (n being an integer, $n = 1, 2, 3...$), a clear signature of the resonant modes with wavelength $\lambda = 2L/n$ localized in the individual air channels. Interestingly, the dispersion relations also indicate that for the triangular network the odd numbered resonant modes (i.e. $n = 1, 3, 5, ..$) generate acoustic band gaps, highlighted by the grey areas in Fig. 2.1(b).

To understand the dispersion plots reported in Fig. 2.1, we first note that, in general, a localized resonant mode tends to hybridize with any propagating wave mode near the resonant frequency[46], resulting in the formation of a band gap due to the avoided crossing (see dashed red lines and shaded red area in Fig. 2.2(a)). However, an exception occurs if the wave mode orthogonal to the resonant one can propagate in the system, since the lack of any possible coupling between the two modes prevents the hybridization process. As a result, a true crossing between the two bands arises (see

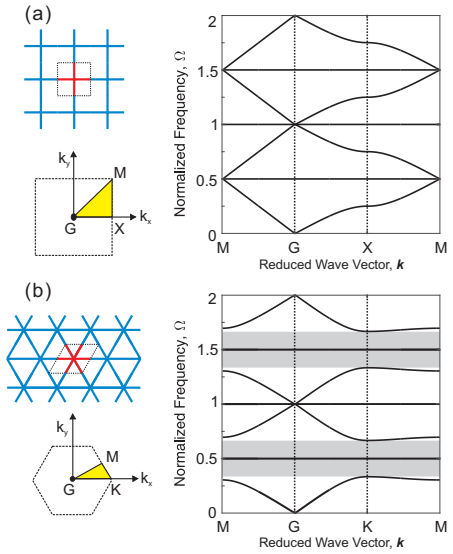

Figure 2.1: Acoustic networks comprising a periodic array of narrow air channels: (a) square lattice and (b) triangular lattice. Lattice configurations, unit cells (highlighted in red) and Brillioun zones are shown on the left. The calculated dispersion relations are shown on the right. The grey regions in (b) highlight the hybridization band gap induced by geometric frustration.

intersections between solid red and blue/green lines in Fig. 2.2(a)) and no gap is formed.

Next, we apply this argument to the square and triangular acoustic networks. To this end, we start by focusing on the resonant modes of the air column enclosed by a single channel. Since both ends of the each channel are open, the pressure field of the fundamental resonant mode is given by $p(x) = p_0 \sin(\pi x/(2L))$ (p_0 being a constant and $x \in [0, L]$) and is symmetric with respect to the center of the tube (see Fig. 2.2(b)). Consequently, the mode orthogonal to the fundamental one at the same frequency/wavelength is anti-symmetric, $p(x) = p_0 \cos(\pi x/(2L))$ (see Fig. 2.2(c)). While this orthogonal mode can be supported by the square network (Fig. 2.2(d)), it is not compatible with the triangular lattice (Fig. 2.2(e)), so that the system becomes frustrated. Importantly, our numerical results indicate that such frustration results in the formation on an hybridization band gap at $\Omega = 0.5$ - a phenomenon that has never been reported before.

In addition, we note that the absence of band gap in the vicinity of the flat band at $\Omega = 1.0$

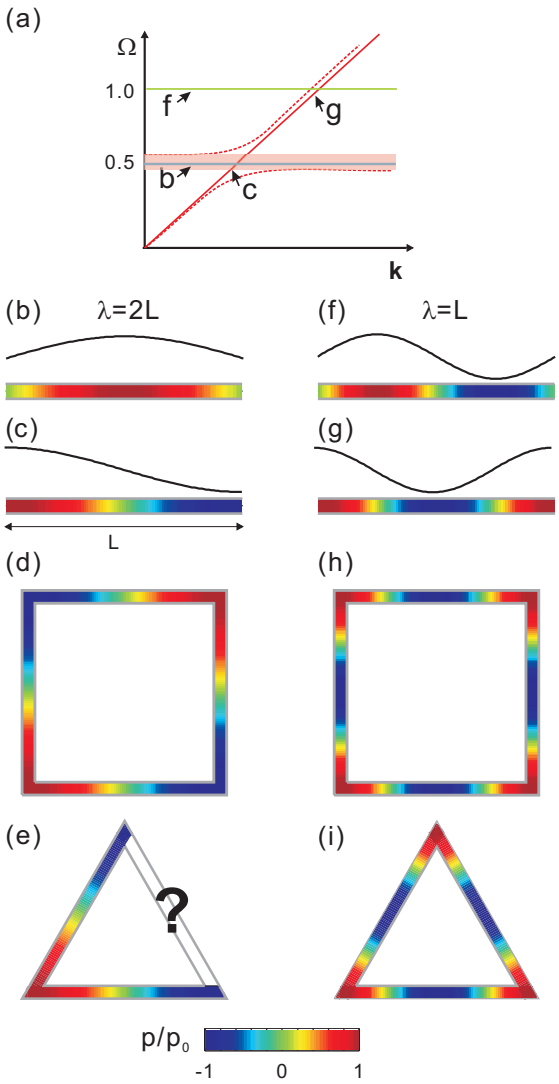

Figure 2.2: Geometric frustration in acoustic networks: (a) schematic of the dispersion relation of an acoustic network showing the formation of an hybridization gap at $\Omega = 0.5$ due to avoided crossing (dotted red lines) and the suppression of the gap at $\Omega = 1.0$ due to true crossing (intersection between solid red and green lines); (b) pressure distribution associated to the fundamental mode for the air column enclosed by a single channel with open ends; (c) wave mode orthogonal to the fundamental one for a single channel with open ends; the orthogonal mode shown in (c) can be supported by (d) the square network, but cannot be supported by (e) the triangular network, so that the system becomes frustrated; (f) pressure distribution associated to the second mode for the air column enclosed by a single channel with open ends; (g) wave mode orthogonal to the second one for a single channel with open ends; the orthogonal mode shown in (g) can be supported by both the (h) square and (i) triangular lattices.

is due to the fact that the mode orthogonal to the second resonant one can be supported by both the square and triangular networks. In fact, the pressure field of the second resonant mode for the individual channels, $p(x) = p_0 \sin(\pi x/L)$, is anti-symmetric with respect to the center of the channel (Fig. 2.2(f)), so that the orthogonal mode, $p(x) = p_0 \cos(\pi x/L)$, is symmetric (Fig. 2.2(g)). It is easy to see that such orthogonal mode is geometrically compatible with both the square (Fig. 2.2(h)) and triangular (Fig. 2.2(i)) networks, as well as any other equilateral lattice geometry. As a result, no locally resonant gap appears at $\Omega = 1.0$ in any acoustic network.

At this point, we also highlight the fact that the formation of locally resonant band gaps induced by geometric frustration is a robust phenomenon. In fact, although in Fig. 2.1 we focus only on the square and triangular geometry, we have also investigated the wave propagation in a number of other acoustic networks and found that any lattice comprising triangles or pentagons is characterized by frustration induced acoustic band gaps (see Fig. S1 in Appendix A). Moreover, while the results presented in Fig. 2.1 are for ideal acoustic networks made of 1D channels, we have also investigated the effect of the finite width t of the tubes. To this end, we have performed FE simulations using the commercial package ABAQUS/Standard and studied the dynamic response of lattices comprising 2D rectangular channels of length L and width t meshed with 4-node bilinear acoustic elements (ABAQUS element type AC2D4). The calculated band structures for the square and triangular networks characterized by $L/t = 20$ are reported in Figs. 2.3(a) and (b), respectively, and show that the dynamic response of the system is not significantly affected by the finite-width of the channels (additional numerical results for networks comprising tubes with different values of L/t are reported in Fig. S2 of Appendix A).

We also conduct steady-state analysis to calculate the transmission of finite size networks comprising 6×6 unit cells made of 2D rectangular channels with $L/t = 20$. In these simulations an harmonic input pressure, p_{input}, is applied at the end of the central channel on the left edge of the model. In Fig. 2.4 we report the steady-state pressure fields obtained for the square and triangular

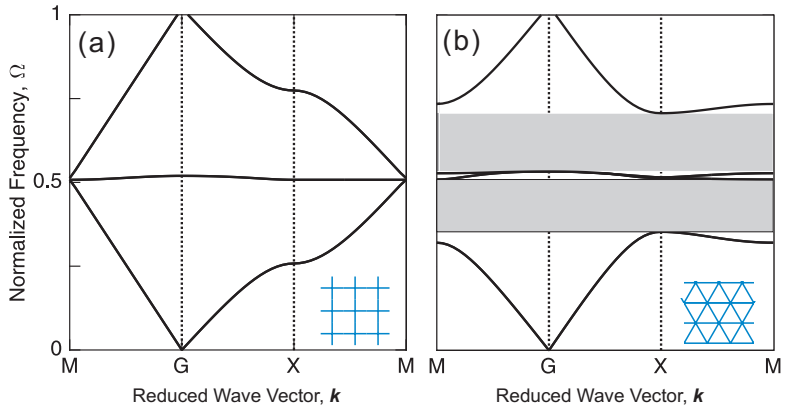

Figure 2.3: Effect of the finite width t of the channels: band structures for (a) the square and (b) the triangular networks characterized by $L/t = 20$. The grey regions in (b) highlight the hybridization band gap induced by geometric frustration.

networks at $\Omega = 0.45$ (in the gap induced by geometrical frustration in the triangular network) and $\Omega = 0.95$ (in the vicinity of the second resonant frequency of a single channel). The results show that in the triangular network at $\Omega = 0.45$ the acoustic energy is completely localized near the excitation site and no signal is transmitted to the opposite end of the lattice (Fig. 2.4(c)) - a clear indication of a band gap. Differently, in all other cases the acoustic waves are found to propagate through the networks (Figs. 2.4(a), (b) and (d)).

Finally, to validate the numerical predictions, we fabricate samples of the square and triangular acoustic networks comprising 6×6 unit cells (Figs. 2.5(a) and (b)). The individual air channels have length $L = 40$ mm, a square cross-section of 2×2 mm (so that $L/t = 20$ and $\omega_1 = 4$ kHz) and are engraved into an acrylic plate of thickness 8 mm with the use of a laser etching machine (KT150, Kern Laser Systems). A flat acrylic plate is then glued on the top of the etched plate to cover the air channels. During the all the experiments, the sample is surrounded with sound-absorbing foams to minimize the effect of the ambient noise. Moreover, an open channel on one of the edges of the samples is connected to an input chamber containing an earphone (352C22, PCB Piezotronics) to excite a broadband white noise signal between 1 kHz and 8 kHz and a microphone to measure the

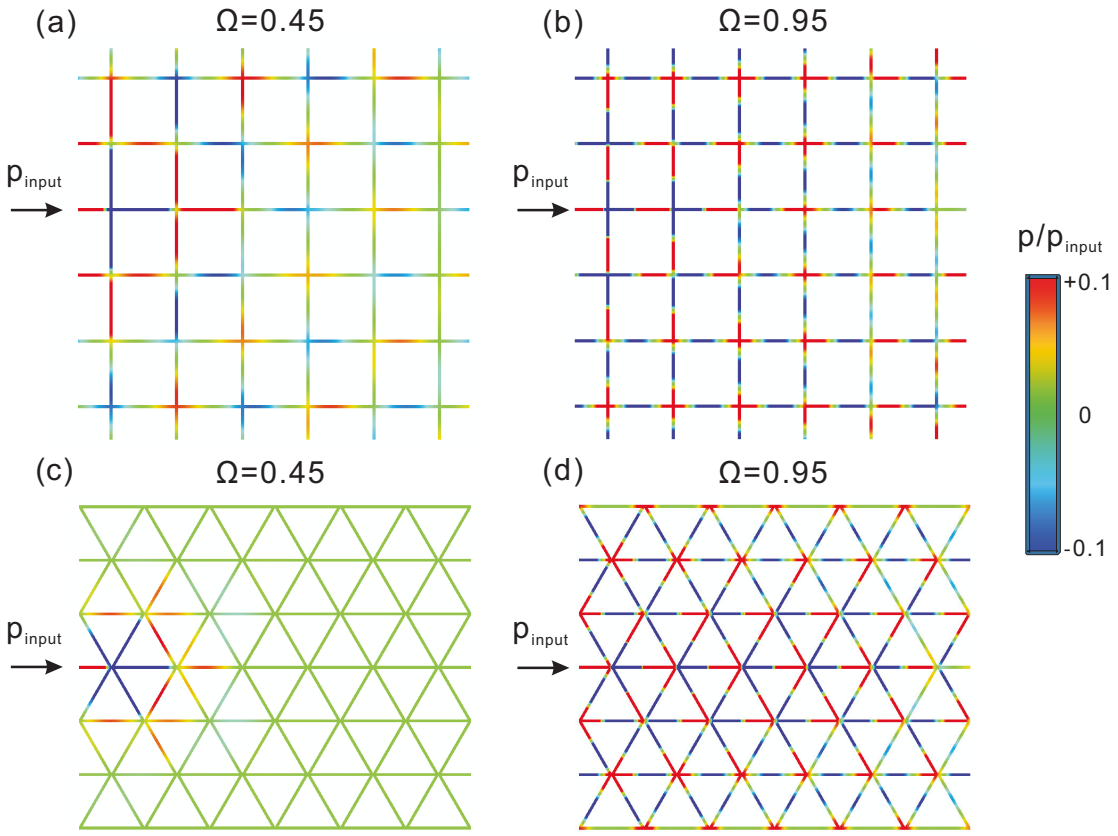

Figure 2.4: Pressure field distribution in finite-sized acoustic networks comprising 6×6 unit cells: (a) square lattice at $\Omega = 0.45$, (b) square lattice at $\Omega = 0.95$, (c) triangular lattice at $\Omega = 0.45$ and (d) triangular lattice at $\Omega = 0.95$. The color indicates the pressure amplitude normalized by the input signal amplitude (p_{input}).

amplitude of the generated sound waves. Another microphone is then placed at an air channel opening on the opposite side of the sample to detect the transmitted signal and the acoustic transmittance is calculated as the ratio between the pressure amplitudes detected by the two microphones (i.e. p_{output}/p_{input}).

The continuous red lines in Figs. 2.5(c) and (d) show the experimentally measured transmittance for the square and triangular sample, respectively, while the blue dashed lines correspond to the transmittance as predicted by steady-state FE simulations. First, we note that the transmittance for the square lattice does not show regions of significant attenuation and fluctuates around -30 dB for experimental data and around -20 dB for numerical results. Such low baseline value is mainly attributable to the dispersion of vibrational energy through the channel openings on the edges, while the 10 dB difference between experimental and numerical results is due to the dissipation in the viscous boundary layers[133], an effect which is not accounted for in the FE simulations. Differently, for the triangular network a significant drop (up to ~ -60 dB) in the transmittance is observed between 2.5 kHz and 6 kHz (i.e. for Ω between 0.3 and 0.7), confirming the existence of the band gap induced by geometric frustration predicted by our analysis.

In summary, we demonstrated both numerically and experimentally that geometric frustration can be exploited to control the propagation of sound waves in networks of narrow air channels. In fact, we found that in acoustic networks comprising triangles or pentagons sonic band gaps emerge in the vicinity of the odd numbered resonant frequencies of the individual channels because of geometric frustration. Remarkably, while sonic band gaps have been previously achieved either by Bragg scattering in ordered arrays of solid inclusions in air[108,55,73,104,100] or by mode hybridization in channels with embedded resonators[112,139,44,32], our results reveal a new mechanism to suppress the propagation of sound waves in specific frequency ranges. We also note that the frustration-induced band gaps demonstrated in this study are characterized by a very peculiar feature: although they are the result of resonance hybridization, their presence completely depend on the lattice geometry.

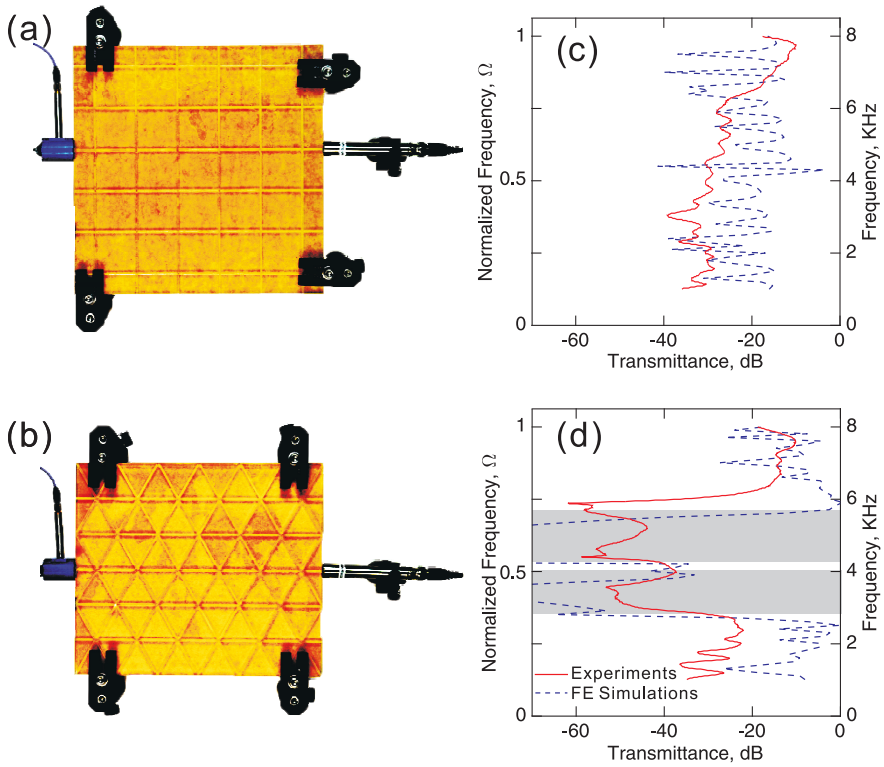

Figure 2.5: Transmittance of finite-sized networks: fabricated samples with (a) the square and (b) triangular networks. The input chamber is connected to the left edge of the samples, while the microphone to measure the amplitude of the generated sound waves is attached to the right edge. The frequency-dependent transmittances for the samples are shown in (c) and (d) for the triangular and square network, respectively. Both experimental (continuous red lines) and numerical (dashed blue line) results are shown. The grey regions in (d) highlight the hybridization band gap as predicted for the corresponding infinite structure (see Fig. 2.1(b)).

This makes them very different from the locally resonant band gaps previously observed in metamaterials comprising embedded resonators[112,68,139,44,32,57], since those have been shown not to be affected the spatial arrangement of resonators[67,125], and also to be retained in the case of randomly distributed resonators[6]. Given the broad range of applications recently demonstrated for systems with acoustic band gaps, including wave guiding[101,148], frequency modulation[49,91], noise reduction[77] and acoustic imaging[63,149,82], we expect geometrically frustrated acoustic networks to play an important role in the design of the next generation of materials and devices that control the propagation of sound.

The important thing in science is not so much to obtain new facts as to discover new ways of thinking about them.

William Henry Bragg

3

Band Gap by Connectivity

The content of this chapter was published in: *Wang P, Casadei F, Kang SH, Bertoldi K. Locally resonant band gaps in periodic beam lattices by tuning connectivity. Physical Review B. 2015;91:020103(R)*[124].

Lattice structures have long fascinated physicists and engineers not only because of their outstanding functionalities, but also for their ability to control the propagation of elastic waves. While the study of the relation between the connectivity of these systems and their static properties has a long history that goes back to Maxwell. However, rules that connect the dynamic response to the network topology have not been established. Generally speaking, the topology of structures comprising a interconnected network of elastic beams can be effectively described by the coordination number ($\bar{z}$), which is defined as the average number of connections at joints. From a static point of view, reducing $\bar{z}$ makes the structure less rigid until a critical threshold is reached, below which deformation modes of zero energy emerge[75,1,87,136,72]. A global stability criterion that purely depends on $\bar{z}$ was first determined by Maxwell for pin-joined lattices comprising spring-like ligaments[75], and then modified to account for the nature (pin or welded) of the joints[94], the bending stiffness of the struts[36,12], self-stresses[16], dislocation defects[90], collapse mechanisms[47] and boundary modes[92,120,114,50]. In recent years, the dynamic response of periodic lattices has also attracted considerable interest[76,59,24,46] because of their ability to tailor the propagation of elastic waves through directional transmissions[101,93,111,19] and band gaps (frequency ranges of strong wave attenuation)[74,93,111,19]. However, though several studies have shown that the wave propagation properties of periodic lattices are highly sensitive to the architecture of the network[101,74,93,111,19], a global criterion connecting the frequency and size of band gaps to the lattice topology is still not yet in place.

In this letter, we study the effects of both the global coordination number ($\bar{z}$) and the local geometric features of periodic networks made of slender beams with finite bending stiffness on the propagation of elastic waves. We consider two dimensional periodic lattices made of Euler-Bernoulli beams supporting both bending and axial deformations. Each beam is made of a linear elastic isotropic material, has length L, mass per unit length m, bending stiffness EI, axial stiffness EA and is characterized by a slenderness ratio $\lambda = L\sqrt{EA/(EI)} = 20$. However, it is important to note that all results presented in the paper are not affected by this specific choice of λ and that identical

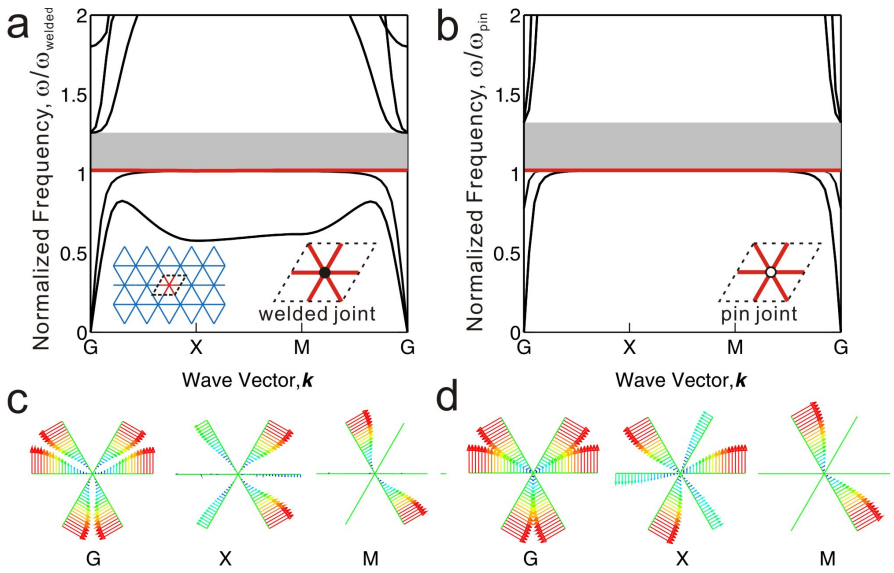

Figure 3.1: Band structures of triangular periodic beam lattices. (a) Dispersion relation of the triangular lattice with welded joints. (b) Dispersion relation of the triangular lattice with pin joints. The lattice and unit cells with both welded and pin joints are shown as insets. Bandgaps are shown as grey-shaded areas and the flat bands at their lower edge are highlighted in red. The Bloch modes of the flat band (the third mode) at high symmetry points of the *Brillouin zone* (G, X and M, see Appendix B) are shown in (c) and (d) for the case of welded and pin joints, respectively. A plot presenting both band structures normalized by the same factor is included in Appendix B

findings can be obtained for network of beams characterized by any value of $\lambda > 10$. To study the propagation of small amplitude elastic waves in such lattices, we perform frequency-domain wave propagation analysis[127,125] within the finite element (FE) framework using the commercial package Abaqus/Standard and Bloch-type boundary conditions are applied to the edges of the unit cell. We then solve the frequency-domain wave equation for wave vectors in the *Brillouin zone* using a perturbation method. Details are given in Appendix B.

We start by investigating the propagation of elastic waves in the triangular lattice (characterized by connectivity $\bar{z} = 6$) with both pin and welded joints. Figures 3.1a and 3.1b show the band structures in term of the normalized frequency ω/ω_{welded} and ω/ω_{pin}, where $\omega_{welded} = 22.4\sqrt{EI/(mL^4)}$ and $\omega_{pin} = \pi^2\sqrt{EI/(mL^4)}$ are the first natural frequency of the a single beam with both ends fixed (welded) and free to rotate (pin), respectively. As previously predicted[93], the dispersion relations indicate that the structure is characterized by a band gap. However, while such band gap is believed to be due to Bragg scattering, our analysis surprisingly indicates that it is generated by localized resonance, a fact that has not been clearly pointed out before. This important observation is clearly supported by the fact that, regardless of the type of joints, the band at the lower edge of the band gap is completely flat (see red lines in Figs. 3.1a and 3.1b) and located in correspondence of the first natural frequency of the beams (i.e. $\omega/\omega_{welded} = 1$ and $\omega/\omega_{pin} = 1$). Furthermore, the Bloch mode shapes of the flat band at the high-symmetry points G, X and M reported in Figs. 3.1c and 3.1d confirm that each beam vibrates independently according to its natural mode. As a result, the vibration energy is localized by the single-beam resonant mode, preventing the propagation of the elastic waves. In previous studies, the local resonance mechanism was typically realized in heterogeneous systems comprising two[122,27,125], three[68,135,67] or four[57] different constituent materials. Remarkably, in periodic triangular lattices, even with a single material and building block, local resonances can be exploited to generate band gaps, providing a foundation for the design of a new class of systems to manipulate the propagation of elastic waves. Furthermore, our results also demonstrate that, in or-

der to attenuate the propagation of elastic waves through localized resonances, it is not necessary to embed additional resonating components[74,143,142,141,38,66,65,138,132,98,19] within the beam lattices. Such single-building-block and single-material system with locally resonant band gap has been previously realized in one-dimensional setup only[53].

Having demonstrated that the triangular beam lattice is characterized by a locally resonant band gap regardless of the type of joints, we now investigate the dynamic response of the hexagonal lattice, which has the same lattice symmetries of the triangular lattice but a much smaller coordination number (i.e. $\bar{z} = 3$). As shown in Fig. 3.2a, the hexagonal lattice with welded joints also exhibits an almost flat band at the resonant frequency of the beams (i.e. $\omega = \omega_{welded}$). However, in this case the flat-band resonant mode does not open a band gap regardless of the types of joints (identical behavior is found in the case of pin joints, as shown in Appendix B). By comparing to the triangular lattice, we note that the absence of the locally resonant band gap in the hexagonal lattice could arise either because of the low connectivity number $\bar{z}$ or the different angle α between connected beams. To further inspect the contribution of the latter factor, by keeping $\bar{z} = 3$ and varying α from $2\pi/3$ to $\pi/3$, we construct periodic lattices that are topologically equivalent to the hexagonal lattice and study their dynamic response. As clearly shown in Figs. 3.2b- 3.2d, though the phononic band structure evolves significantly as α changes, no band gap is observed. It is especially important to note that for $\alpha = \pi/3$ the beams are arranged exactly as in the triangular lattice. However, the network topology is different, as only three, instead of six, beams connect to each other at each joint (see inset in Fig. 3.2d). Thus, these results conclusively show that the global topology of the network described by the coordination number plays a crucial role in determining the existence of locally resonant band gaps. In addition, our analysis indicates that this conclusion is not affected by the nature of the joints (additional results for pin joints are included in Appendix B).

Next, to further demonstrate the role of the coordination number on the formation of locally resonant band gaps, we investigate a number of periodic beam lattices with $3 < \bar{z} < 6$, as shown

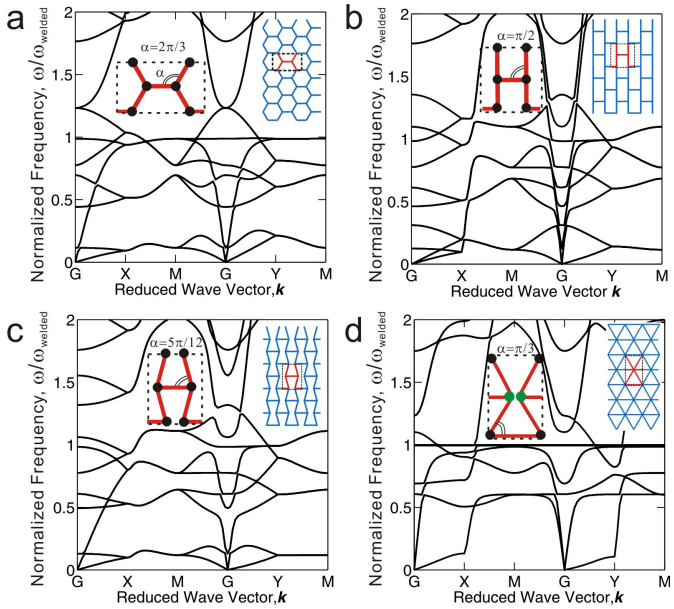

Figure 3.2: Band structure of periodic lattices with $\bar{z} = 3$ and welded joints. (a) Hexagonal lattice ($\alpha = 2\pi/3$); (b) Topologically equivalent lattice with $\alpha = \pi/2$; (c) Topologically equivalent lattice with $\alpha = 5\pi/12$; and (d) Topologically equivalent lattice with $\alpha = \pi/3$. The lattice structures and unit cells used in the calculations are shown as insets. Note that for $\alpha = \pi/3$ the arrangement of the beams is the same as for the triangular lattice, but the connectivity is still $\bar{z} = 3$. In fact, although for clarity the green-colored joints are drawn separately in the unit cell of **d**, they are positioned at the same spatial location. No locally resonant band gap is found for any of the configurations. Results for the same lattices with pin joints are provided in Appendix B.

in Fig. 3.3a. These hybrid lattices are generated by considering enlarged unit cells of the triangular lattice and randomly removing a number of joints and all beams attached to them. Alternatively, lattices with $\bar{z}$ close to 3 are constructed starting with an enlarged unit cell of the hexagonal lattice and filling some randomly chosen hexagons with six triangles. For each value of $\bar{z}$ multiple configurations are analyzed and, since these periodic lattices do not share the same spatial symmetry of the triangular and hexagonal lattices, additional Bloch vectors are considered to determine the presence of band gaps, as detailed in Appendix B. The results are summarized in Fig. 3.3b, where the width of the band gap $\Delta\omega$ is reported for different hybrid lattices with $3 < \bar{z} < 6$. Each circular marker in the plot represents the average gap width of all configurations considered for that particular value of $\bar{z}$, while the corresponding error bar spans the range of observed $\Delta\omega$. Interestingly, for lattices with low connectivity (i.e. $3.0 < \bar{z} < 3.7$ - yellow region in Fig. 3.3b), no locally resonant band gap is observed at $\omega = \omega_{welded}$.

In contrast, when $4.6 < \bar{z} < 6.0$ (red region in Fig. 3.3b), all considered lattices possess a locally resonant band gap. In particular, for structures with a very high average connectivity (i.e. $\bar{z} > 5.5$), the band gap width $\Delta\omega$ is linearly correlated to the coordination number $\bar{z}$. On the other hand, if $4.6 < \bar{z} < 5.7$, although a locally resonant band gap always exists, its size is not solely determined by $\bar{z}$, but also affected by the specific arrangement of the beams within the unit cell. Finally, when $3.7 < \bar{z} < 4.6$ (orange region in Fig. 3.3b), depending on the local geometric features, the lattice may either have or not have a locally resonant band gap.

The results presented in Fig. 3.3 not only confirm that the global topology of the lattice is the leading factor in determining the existence of a locally resonant band gap, but also indicate that for an intermediate range of $\bar{z}$ the detailed geometry of the lattice plays an important role. To further understand the effect of the arrangement of the beams in lattices characterized by intermediate values of $\bar{z}$, we also study rhombic lattices with $\bar{z} = 4$ and investigate the effect of the angle ϑ between the beams at the joints. We start from the case of $\vartheta = \pi/2$, the well-known square lattice, which

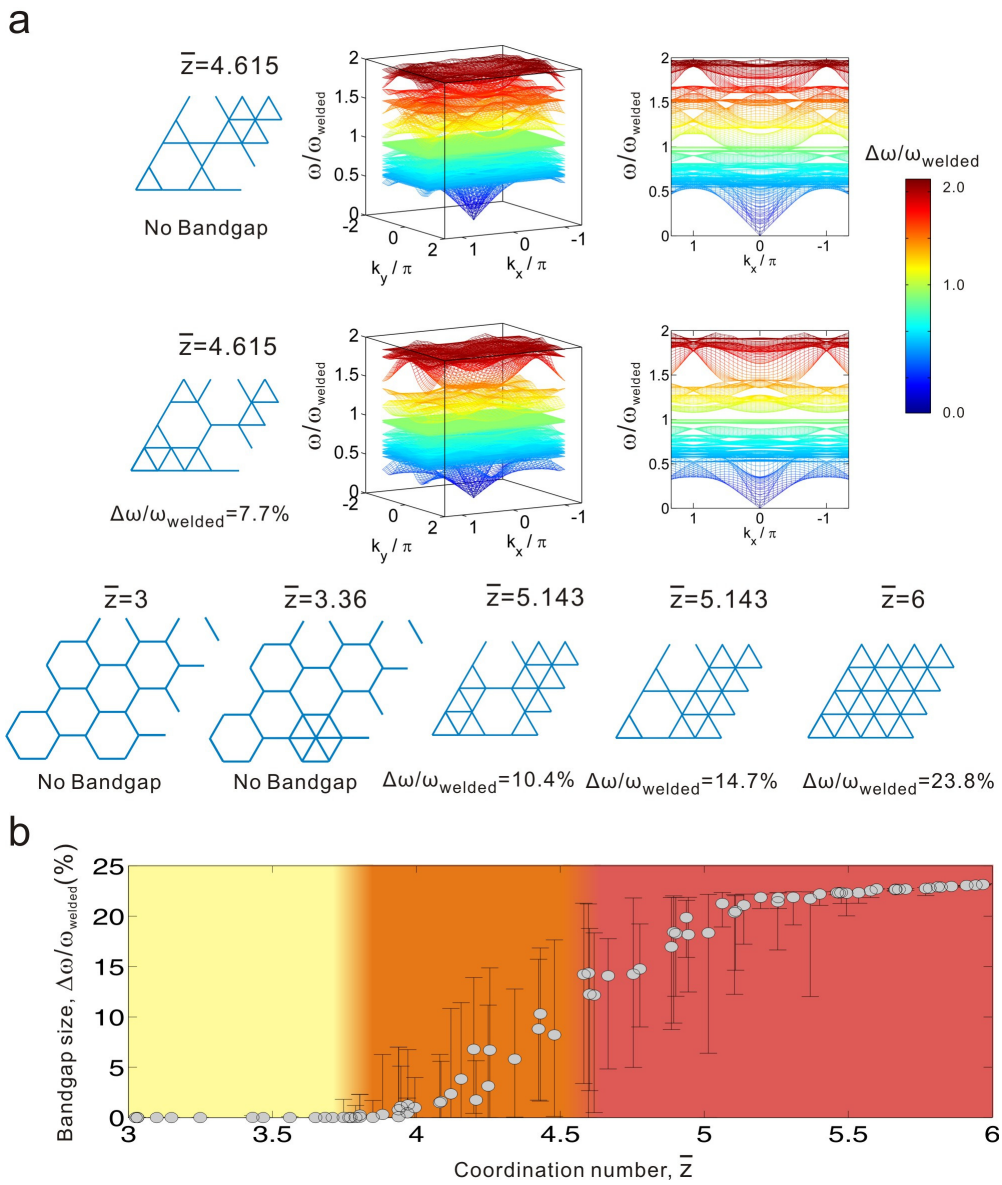

Figure 3.3: Dynamic response of periodic lattices with $3 < \bar{z} < 6$. (a) Representative unit cells constructed either starting from the triangular lattice and removing a number of randomly chosen nodes or starting from the hexagonal lattice and filling a number of randomly chosen hexagons with six triangles. For two unit cells with $\bar{z} = 4.615$ also the band structures are shown. **b,** Relation between normalized average band gap size $\Delta\omega/\omega_{welded}$ and coordination number $\bar{z}$. The band gap size is computed as the difference between the upper and lower edges of the gap. The error bar at each data point indicates the band gap range of frequencies spanned by all different configurations characterized by the same value of $\bar{z}$.

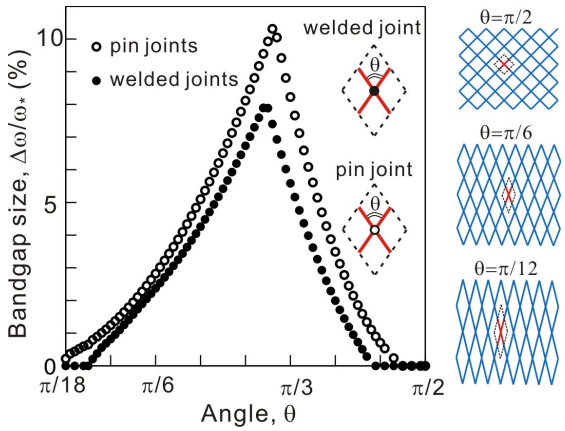

Figure 3.4: Normalized band gap width $\Delta\omega/\omega_*$ for rhombic lattices that are topologically equivalent to the square lattice. The lattice structures and joint types used in the calculations are shown as insets. The results for lattices with both welded and pin joints are reported. Note that $\omega_* = \omega_{welded}$ and $\omega_* = \omega_{pin}$ for lattices with welded and pin joints, respectively.

does not have a locally resonant band gap[93]. However, as shown in Fig. 3.4, when the angle ϑ is progressively reduced, a locally resonant band gap appears for rhombic lattices. Interestingly, we also find that a maximum band gap width is achieved for $\vartheta = 56\pi/180$, regardless of the joint types. Therefore, our results indicate that, when extended to the dynamic response of the beam lattices, Maxwell's rule can be relaxed. In fact, while $\bar{z} = 4$ represents the critical threshold below which a lattice made of spring-like ligaments becomes unstable, the rhombic lattices at the threshold can still possess a locally resonant band gap by carefully choosing the angle ϑ.

In summary, we have numerically investigated the dynamic response of periodic beam lattices. We have found that, in highly connected lattices, the beams themselves act as mechanical resonators, enabling the generation of locally resonant band gaps. Similar to the observation reported for the effective static properties of lattices[75,72,94,12,120,114], our results indicate that the presence and width of the locally resonant band gap depends on the coordination number (i.e. average lattice connectivity, $\bar{z}$). A reduction of $\bar{z}$ results in a decrease of the band width, until a critical threshold is reached, below which the band gap completely closes. On the other hand, we have found that, different from

the ground state static properties[94,36,11], the dynamic response of the system is not sensitive to the type of joints. Under dynamic loading, the lattices are in an excited state characterized by a finite level of energy, and the response is not qualitatively affected by the bending stiffness of the joints. Moreover, we have also shown that the average connectivity is not enough to predict the dynamic characteristics of a system when $\bar{z}$ is near the critical threshold. In fact, we identified a transition region where the dynamic response of the lattices is sensitive to the detailed architecture of the network. Our work paves the way towards the design of a new class of systems made of identical elastic beams that can effectively attenuate the propagation of elastic waves at low frequencies by exploiting local resonances. As an example, highly connected periodic lattices with beam length $\sim$ 40 mm, thickness $\sim$ 2.0 mm, which are made of an acrylic polymer that can be easily 3D-printed (Young's modulus $\sim$ 1.14 GPa, density $\sim$ 1050 kg/m^3), exhibit a locally resonant band gap in the audible frequency range (i.e. at around 590 Hz and 1340 Hz for the case of pin and welded joints, respectively).

No, no. These concepts (topological bundle theory) were not dreamed up.

They were natural and real.

Shiing-Shen Chern

God made the bulk; surfaces were invented by the devil.

Wolfgang Pauli

4

Topological Band Gap

The content of this chapter was published in: *Wang P, Lu L, Bertoldi K. Topological Phononic Crystals with One-Way Elastic Edge Waves. Physical Review Letters. 2015;115:104302*[126].

Topological states in electronic materials, including the quantum Hall effect[121] and topological insulators[43,96], have inspired a number of recent developments in photonics[40,69], phononics[95,146,115,137] and mechanical metamaterials [114,50,90,21]. In particular, in analogy to the quantum anomalous Hall effect[39], one-way electromagnetic waveguides in two-dimensional systems have been realized by breaking time-reversal symmetry[131,130,110,109].

Very recently unidirectional edge channels have been proposed for elastic waves using Coriolis force in a non-inertial reference frame[129], but such a rotating frame is very difficult to implement in solid state devices. Moreover, one-way propagation of scalar acoustic waves has also been proposed by introducing rotating fluids[34,140,86]. However, it is important to recognize that elastic waves in solids have both transverse and longitudinal polarizations, while acoustic waves in fluids are purely longitudinal. As a result, it is challenging to achieve topological protection for elastic waves on an integrated device platform.

Here, we present a robust strategy to create topologically nontrivial edge modes for both longitudinal and transverse polarizations in a solid medium. In particular, we introduce gyroscopic phononic crystals, where each lattice site is coupled with a spinning gyroscope that breaks time-reversal symmetry in a well-controlled manner. In both hexagonal and square lattices, gyroscopic coupling opens band gaps that are characterized by Chern numbers of 1 and 2. As a result, at the edge of these lattices both single-mode and multi-mode one-way elastic waves are observed to propagate around arbitrary defects without backscattering.

To start, we consider a hexagonal phononic crystal with equal masses ($m_2 = m_1$) connected by linear springs (red and black rods in Figs. 4.1a and 4.1b). The resulting unit cell has four degrees of freedom specified by the displacements of m_1 and m_2 ($\mathbf{U} = [u_x^{m_1}, u_y^{m_1}, u_x^{m_2}, u_y^{m_2}]$). Consequently, there are a total of four bands in the band structure (Fig. 4.1c). Note that this is the minimal number of bands required to open a complete band gap, since the first two elastic dispersion bands are pinned at zero frequency. The phononic band structures are calculated by solving the dispersion

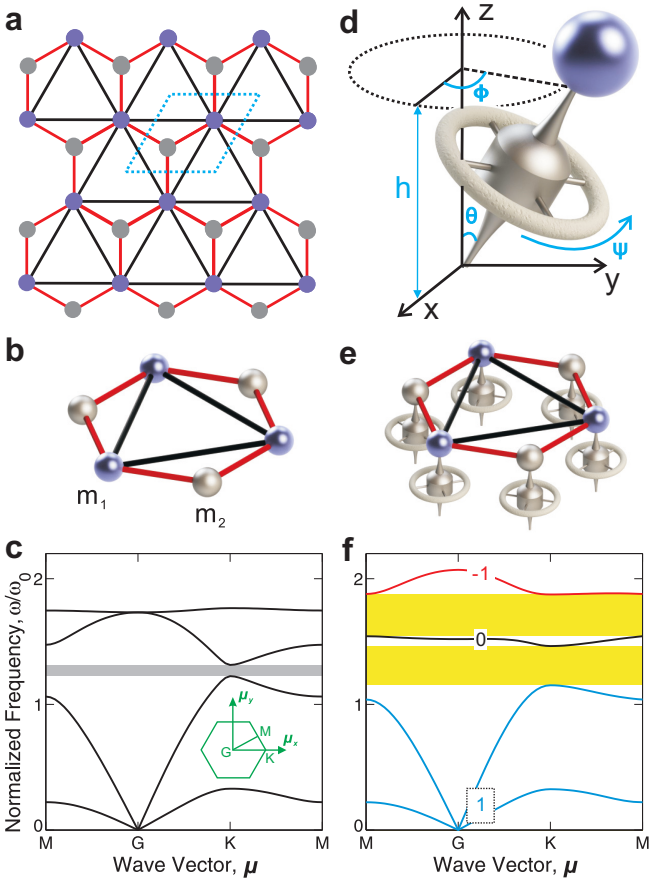

Figure 4.1: Ordinary and Gyroscopic Phononic Crystals: (a) Schematic of the hexagonal lattice. The blue and grey spheres represent concentrated masses m_1 and $m_2 = m_1$, respectively. The red and black straight rods represent mass-less linear springs with stiffness k_1 and $k_2 = k_1/20$, respectively. The dashed cell is the primitive cell of the lattice. **(b)** Unit cell for the ordinary (non-gyroscopic) phononic crystal. **(c)** Band structure of the ordinary (non-gyroscopic) phononic crystal. The inset is the Brillouin zone. **(d)** Schematic of a gyroscope with the top tip pinned to a mass in the lattice. **(e)** Unit cell for the gyroscopic phononic crystal. **(f)** Band structure of the gyroscopic phononic crystal ($\alpha_1 = \alpha_2 = 0.3m_1$) with the Chern numbers labeled on the bulk bands. The frequencies are normalized by $\omega_0 = \sqrt{k_1/m_1}$.

equation [46]

$$[\mathbf{K}(\mu) - \omega^2\mathbf{M}]\,\mathbf{U} = 0 \tag{4.1}$$

for wave vectors μ within the first Brillouin zone. Here, ω denotes the angular frequency of the propagating wave and $\mathbf{M} = \mathrm{diag}\{m_1,\ m_1,\ m_2,\ m_2\}$ is the mass matrix. Moreover, $\mathbf{K}$ is the 4×4 stiffness matrix and is a function of the Bloch wave vector μ. The band structure of this simple lattice is shown in Fig. 4.1c. As expected, in the long wavelength regime (near *G*-point) the first and second bands correspond to transverse and longitudinal modes, respectively, while for short wavelengths (near *K*-points) all modes are found to have mixed polarization (detailed analysis of the modal polarization is given in Appendix C). Moreover, we observe a quadratic degeneracy between the third and fourth bands at the center of the Brillouin zone and a complete gap between the second and third bands due to the lack of inversion symmetry. However, this gap is topologically trivial, since time-reversal symmetry is not broken and the Chern numbers of the bands are all zero.

In order to break time-reversal symmetry, we introduce gyroscopic coupling [80,14,17] and attach each mass in the lattice to the tip of the rotational axis of a gyroscope, as shown in Fig. 4.1d. Note that the other tip of the gyroscope is pinned to the ground to prevent any translational motion, while allowing for free rotations. Because of the small-amplitude in-plane waves propagating in the phononic lattice, the magnitude of the tip displacement of the each gyroscope is given by

$$U_{tip} = h\sin\vartheta \approx h\vartheta = h\Theta e^{i\omega t} \quad \text{for} \quad |\Theta| \ll 1, \tag{4.2}$$

where h and ϑ denote the height and nutation angle of the gyroscope (Fig. 4.1d) and Θ is the amplitude of the harmonic change in ϑ. Interestingly, the coupling between the mass in the lattice and the gyroscope induces an in-plane gyroscopic inertial force perpendicular to the direction of U_{tip} [14,37]:

$$F_g = \pm i\omega^2\alpha U_{tip}, \tag{4.3}$$

where α is the spinner constant that characterizes the strength of the rotational coupling between two independent inertias in the 2D plane. As a result, the mass matrix in Eq. (4.1) becomes,

$$\tilde{\mathbf{M}} = \mathbf{M} + \begin{pmatrix} 0 & i\alpha_1 & 0 & 0 \\ -i\alpha_1 & 0 & 0 & 0 \\ 0 & 0 & 0 & i\alpha_2 \\ 0 & 0 & -i\alpha_2 & 0 \end{pmatrix}, \tag{4.4}$$

where α_1 and α_2 denote the spinner constants of the gyroscopes attached to m_1 and m_2, respectively. We note that the imaginary nature of the gyroscopic inertial effect indicates directional phase shifts with respect to the tip displacements, which breaks time-reversal symmetry.

We now consider the band structure of the gyroscopic hexagonal lattice. Interestingly, we find that the original band gap between the second and third bands first closes into a Dirac cone at the *K*-points and then reopens as we gradually increase the magnitude of α_1 and α_2. In particular, for $\alpha_1 = \alpha_2 = 0.07m_1$ the gap is closed and a pair of Dirac cones at *K*-points emerges, while for $\alpha_1 = \alpha_2 = 0.3m_1$ the gap reopens, as shown in Fig. 4.1f. We also note that this topological transition at $\alpha_1 = \alpha_2 = 0.07m_1$ is accompanied by a band inversion[137] between the second and third bands near the *K*-points (the complete process of this topological transition is shown in the Appendix C). Since each Dirac point carries a Berry phase of π and there is a pair of Dirac cones in the first Brillouin zone [*], we expect the total exchange of Berry curvature between the two bands to be 2π, resulting in one chiral edge state in the gap between the second and third bands. Similarly, we also observe that the quadratic degeneracy found for the ordinary lattice between the third and fourth bands at the Brillouin zone center (see Fig. 4.1c) is opened into a full band gap when gyroscopic coupling is introduced (see Fig. 4.1f). Since such a quadratic touching carries a 2π Berry phase[25],

[*] Note that on the boundary of the first Brillouin zone of the hexagonal lattice there are six Dirac points. However, since at each point only one third of the Dirac cone is included in the first Brillouin zone, we have a pair of Dirac cones in total.

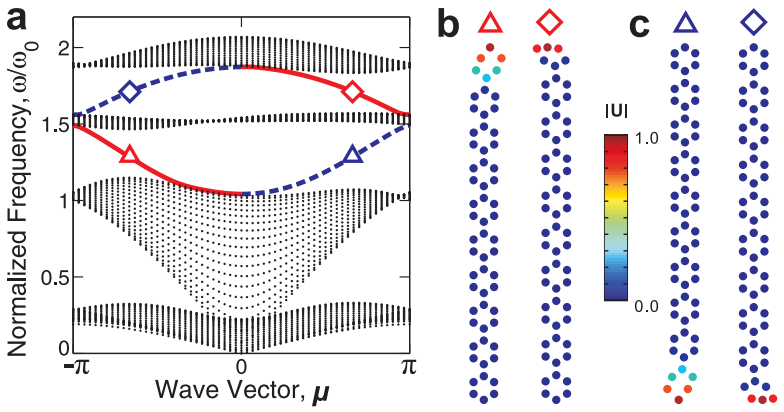

Figure 4.2: Edge modes in Gyroscopic Phononic Crystal: (a) 1D band structure showing bulk bands (black dots) and edge bands (colored lines). Red solid lines represent edge modes bound to the top boundary, while blue dashed lines represent edge modes bound to the bottom boundary. **(b)** Modal displacement fields of top edge states with negative group velocities. **(c)** Modal displacement fields of bottom edge states with positive group velocities

there should be one chiral edge state in the gap between the third and fourth bands. Importantly, the fact that band gaps in Fig. 4.1f are topologically-nontrivial is confirmed by the non-zero Chern numbers labeled on the bands (the calculations conducted to compute these topological invariants are detailed in the Appendix C). Therefore, in the frequency ranges of these nontrivial band gaps, we expect gapless one-way edge states, whose number is dictated by the sum of Chern numbers below the band gap, in agreement with our intuitive arguments of Berry phase.

To verify the existence of such one-way edge states, we perform one-dimensional (1D) Bloch wave analysis on a supercell comprising 20×1 unit cells, assuming free boundary conditions for the top and bottom edges. In full agreement with the bulk Chern numbers, the band structure of the supercell shows one one-way edge mode on each edge in both band gaps. For modes bound to the top edge (Fig. 4.2b), the propagation can only assume negative group velocities (red solid lines with negative slope in Fig. 4.2a). On the other hand, the modes bound to the bottom edge (Fig. 4.2c) possess positive group velocities (blue dashed lines with positive slope in Fig. 4.2a). Since these edge modes are in the gap frequency range where no bulk modes may exist, they cannot scatter into the bulk of the phononic crystal. Furthermore, their uni-directional group velocities guarantee the absence

of any back scattering and result in the topologically protected one-way propagation of vibration energy.

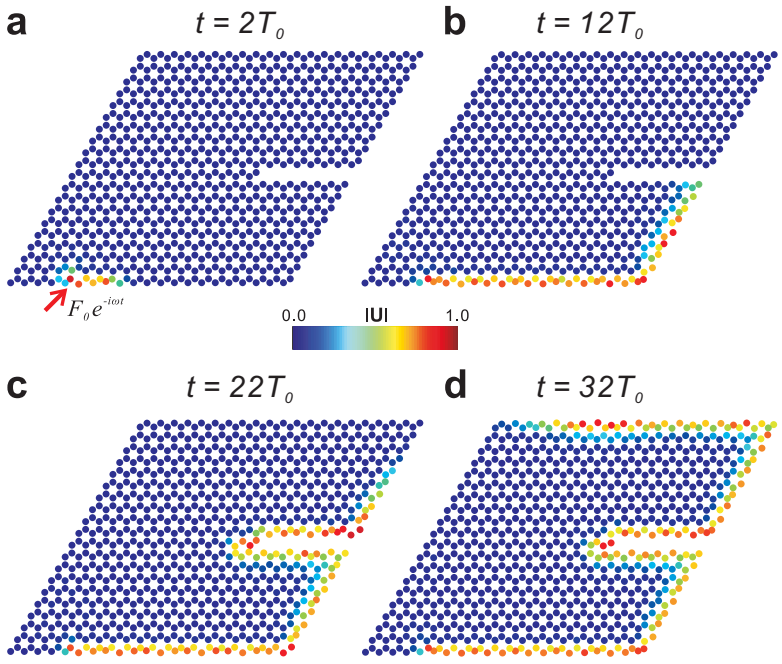

Figure 4.3: Transient Response of a gyroscopic phononic crystal consisting of 20×20 unit cells with a line defect on the right boundary: Snapshots of the displacement field at **(a)** $t = 2T_o$, **(b)** $t = 12T_o$, **(c)** $t = 22T_o$ and **(d)** $t = 32T_o$, where $T_o = \sqrt{m_1/k_1}$ is the characteristic time scale of the system. Starting from $t = 0$, a time-harmonic excitation force $\mathbf{F}(t) = [F_x(t),\ F_y(t)] = [1,\ 1]F_o e^{-i\omega t}$ is prescribed at the site indicated by the red arrow.

To show the robustness of these edge states, we conduct transient analysis on a finite sample comprising 20×20 unit cells with a line defect on the right boundary created by removing twelve masses and the springs connected to them (Fig. 4.3a). A harmonic force excitation, $F_o e^{-i\omega t}$, is prescribed at a mass site on the bottom boundary (red arrow in Fig. 4.3a) with frequency within the bulk band gap between the second and third bands ($\omega/\omega_o = 1.3$). In Fig. 4.3 we plot snapshots of the velocity field at different time instances, $t/T_o = 2$, 12, 22 and 32, where $T_o = \sqrt{m_1/k_1}$ is the characteristic time scale of the system. Remarkably, because of their topological protection, the edge modes circumvent both the sharp corner and the line defect without any reflection. We note that,

although the results presented in Fig. 4.3 are for an harmonic excitation with 45° inclination (i.e. $\mathbf{F}(t) = [F_x(t),\ F_y(t)] = [1,\ 1]F_0 e^{-i\omega t}$), the one-way edge propagations are not affected by the direction of the applied force (additional results are included in the Appendix C).

Next, we investigate the effect of the lattice geometry and start with an ordinary square phononic crystal with masses m_1 connected by springs with elastic constant k_1. To make the lattice statically stable, we add an additional mass $m_2 = m_1$ at the center of each unit cell and connect it to its four adjacent m_1 masses by springs with elastic constant $k_2 = 2k_1$ (See Figs. 4.4a). The band structure for this lattice (shown in Fig. 4.4b) contains a pair of three-fold linear degeneracies among the first, second and third bands at the X points of the Brillouin zone. Note that this type of degeneracy, consisting of a locally flat band and a Dirac point, is known as the "accidental Dirac point" or "Dirac-like cones"[64,45]. Interestingly, while this type of degeneracy was previously found to occur at the Brillouin zone center and very sensitive to the system parameters, in our lattice it robustly appears at the X points when $m_1 = m_2$. Upon the introduction of gyroscopic inertial effects ($\alpha_1 = \alpha_2 = 0.3\, m_1$), these three-fold degenerate points are lifted and a gap is created between the second and third bands (Fig. 4.4c). The Chern numbers of two bulk bands below the gap is two, predicting the existence of two topological edge states. The presence of multi- mode one-way elastic waves is consistent with the fact that the Berry phase associated with such a three-band degeneracy is 2π [78], resulting in a total exchange of Berry curvature of 4π when gapping two of these points in the Brillouin zone [†]. In Figs. 4.4d and 4.4e, we plot the band structure of the corresponding 20×1 supercell, highlighting the two one-way edge modes and their modal displacement fields.

To summarize, we demonstrated that gyroscopic phononic crystals can support topologically non-trivial gaps, within which the edge states are unidirectional and immune to back-scattering. The transient analysis confirmed that the propagations of such topological edge waves are robust

[†]Note that on the boundary of the first Brillouin zone of the square lattice there are four equivalent X-points. However, since at each point only one half of the three-band degeneracy is included in the first Brillouin zone, we have a pair of three-band degeneracies in total.

against large defects and sharp corners. Moreover, we showed, for the first time, the multimode one-way states (Chern number = ± 2) in phononic systems, opening more avenues for the design of future topological waveguides and devices. While in this study we developed a comprehensive framework for the design and analysis of topological phononic crystals, we recently became aware of a parallel effort in which time-reversal symmetry breaking in a gyroscopic system has been theoretically analysed and experimentally demonstrated [85].

Finally, we note that phononic crystals [107,56] and acoustic metamaterials [68,32,30,57,125] that enable manipulation and control of elastic waves have received significant interest in recent years [71,46], not only because of their rich physics, but also for their broad range of applications [101,93,119,49,91,77,13,22,26,60,3,70,29]. Interestingly, the edge wave modes in phononic crystals are important in many scenarios [118,117,5,61], including vibration control [116] and acoustic imaging [26]. However, most of reported studies have focused on topologically trivial surface waves that can be easily scattered or localized by defects [118]. Therefore, the work reported here could open new avenues for the design of phononic devices with special properties and functionalities on edges, surfaces and interfaces.

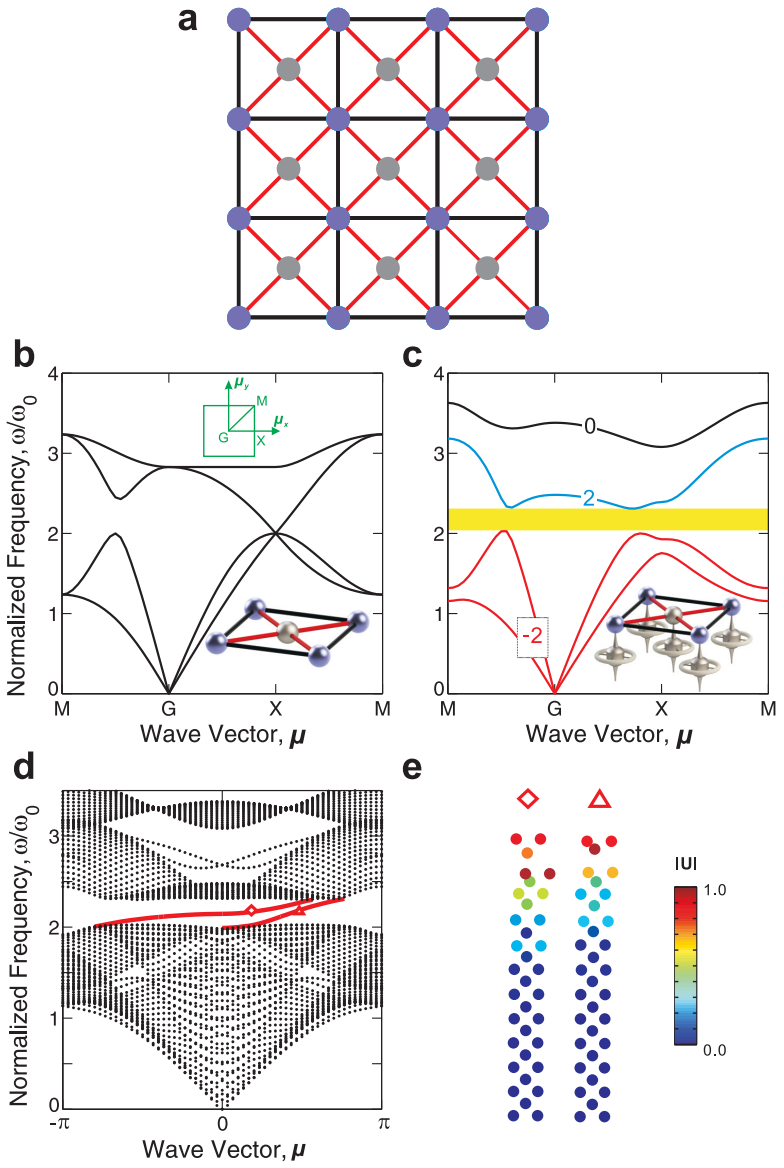

Figure 4.4: Square Lattice results: (a) Schematic of the square lattice. The blue and grey spheres represent concentrated masses m_1 and $m_2 = m_1$, respectively. The black and red straight rods represent mass-less linear springs with stiffness k_1 and $k_2 = 2k_1$, respectively. **(b)** Band structure of the ordinary (non-gyroscopic) phononic crystal. The insets are the Brillouin zone and the unit cell. **(c)** Band structure of the gyroscopic phononic crystal ($\alpha_1 = \alpha_2 = 0.3m_1$) with the Chern numbers labeled on the bulk bands. Frequencies are normalized by $\omega_0 = \sqrt{k_1/m_1}$. The inset is the unit cell. **(d)** 1D band structure showing bulk bands (black dots) and two topological edge bands (red solid lines) bound to the top boundary. Note that the edge bands that are bound to the bottom boundary are not shown here. **(e)** Modal displacement fields of the edge states shown in **(d)**.

Nothing is too wonderful to be true if it be consistent with the laws of nature.

Michael Faraday

A picture is worth a thousand words; an equation is worth a thousand pictures; and an idea is worth a thousand equations!

5

Conclusion

Phononic crystals and acoustic metamaterials provide many opportunities to manipulate sound and vibrations. One of the most interesting of these is their ability to tailor the propagation of acoustic and elastic waves through phononic band gaps - frequency ranges of strong attenuation. Although there have been numerous studies focused on band-gap materials in the last two decades, only two types of gaps have been demonstrated: Bragg-type gaps emerging from the collective scattering and hybridization gaps created by embedded resonators. In this thesis, I report the discoveries of three

new types of phononic band gaps, providing novel strategies for the design of next-generation smart systems with targeted dynamic behavior.

First, as shown in Chapter 2, geometric frustrations in acoustic waveguide networks comprising triangles or pentagons can induce band gaps in the vicinity of the odd numbered resonant frequencies of the individual channels. The numerical and experimental results reveal that this new mechanism is different from that of embedded resonators in two aspects. On one hand, in conventional designs of acoustic metamaterials, there has always been a clear distinction between the bulk matrix material and the resonating unit. Acoustic networks with geometric-frustration gaps, on the contrary, comprise air channels that, surprisingly, function as both the matrix and the resonator. On the other hand, locally resonant band gaps previously observed in metamaterials are not sensitive to the spatial arrangement of resonators, and they can also be retained in the case of randomly distributed resonators. In contrast, the frustration-induced band gaps are fundamentally dependent on the spatial configuration of the air channels and can be completely determined by the lattice geometry. Besides these peculiar features, this study also provides the first demonstration for the geometric frustration of continuous wave function in a macroscopic system which can be easily fabricated and conveniently studied.

Second, band gaps in lattices of structural beams with finite bending stiffness are also found to be a new kind in Chapter 3. Although these gaps have been previously predicted and are well known to the research community, our new results indicate that they are also hybridization gaps caused by the resonance mode of individual beams. Similar to the case of air channels in acoustic waveguide networks, each beam in the lattices actually act as both a part of bulk matrix and an independent resonating unit. This discovery compels the study to focus on the conditions for the formation of the gaps in beam lattices of different configurations. However, the simple argument of geometric frustration can not be directly applied to this case anymore. Since beams can support both axial and flexural deformations, the waves in these lattices are vectorial in nature. Moreover, the flexural

wave on each beam has a quadratic dispersion by itself, which further complicates the problem. Extensive numerical studies eventually unearth the fact that the presence and width of the locally resonant band gap in beam lattices depends on the average lattice connectivity of the network. The gap always exists in lattices with high connectivity, and there is a critical threshold for the average connectivity, from which the gap size is purely dictated by the global lattice topology. However, near this critical value, the detailed local geometry of the lattice also has strong effects. Furthermore, The rotational stiffness of the joints in the network is found to be irrelevant to the dynamic response of the lattices. The new findings discussed here offer guidelines for the optimization of beam networks for dynamic behaviors.

Finally, Chapter 4 provides a phononic analogue of the electronic quantum Hall effect, which gives rise to robust edge states and further leads to the discovery of topological insulators. In particular, gyroscopic effects are introduced into typical two-dimensional phononic lattices comprising point masses and linear springs. Topologically non-trivial phononic gaps for both longitudinal and transverse wave-polarizations are created as a result of time-reversal breaking by gyroscopes. Numerical methods are developed to calculate the topological invariant, Chern number, that characterizes the system. Interestingly, elastic waves bound to the edges in topological phononic crystals are shown to be strictly one-way and robust against any heterogeneity. In addition, multi-mode topological edge waves are demonstrated by changing the configuration of base lattice. It is worth pointing out that, although the spring-mass system investigated in Chapter 4 is nothing more than a minimalistic "toy model", it is fundamental to any topological band gaps, in a way similar to the models shown in Fig. 1.1 of Chapter 1 for conventional types of band gaps. This study of topological phononics provides a new concept and methodology for future scientific studies and technological advances.

To summarize, the two systems discussed in Chapters 2 and 3 are different but related. Both are based on lattice geometries and have resonant band gaps "spotaneously" created by lattice compon-

ent in single-material designs without explicitly embedded resonators. The investigations on these new gap-forming mechanisms, namely geometric frustration and lattice connectivity, can significantly widen the range of possibilities for designing dynamic devices with novel properties in a much simpler way than has been possible so far.

More importantly, the topological phononic band gap discussed in Chapter 4 possess a striking and technologically promising property: the existence of edge waves traveling in a single direction without any possible backscattering, regardless of the existence of defects or disorder. This phenomenon does not occur in any ordinary wave devices, promising novel applications for vibration isolators, modulators, and transducers. In fact, much like the scientific paradigm shift caused by topological insulators in semi-conductor materials for electronics, the study of wave topology represents the new frontier of acoustic technology and will certainly revolutionize the research field in the next few years. Discoveries and inventions in phononic crystals and acoustic metamaterials have all been based on topologically-trivial gaps and wave modes in the last two decades. Now a new topological era awaits.

A

Supplemental Material to Chapter 2

A.1 Calculation of dispersion relations for acoustic networks

A.1.1 Finite Element formulation

In this study we focus on acoustic networks comprising a periodic array of narrow air channels of length L and cross-sectional width t, for which $t << L$. Therefore, in any individual channel the

free vibrations of the enclosed air column can be described by the 1D wave equation [84]

$$\frac{\partial^2 p}{\partial t^2} - c^2 \frac{\partial^2 p}{\partial x^2} = 0, \tag{A.1}$$

where p is the acoustic pressure (the local deviation from the ambient pressure), c is the speed of sound in the channel and $x \in [0,\ L]$ denotes the position along the channel. Since for a periodic network of air channels Eq. (A.1) cannot be solved analytically, we determine its solution numerically by using the finite element (FE) method.

To develop the FE formulation, we start by restating Eq. (A.1) in the weak form. We multiply both terms in Eq. (A.1) by an arbitrary function $w(x)$ and integrate over the domain $[0,\ L]$,

$$\int_0^L w \frac{\partial^2 p}{\partial t^2} dx - c^2 \int_0^L w \frac{\partial^2 p}{\partial x^2} dx = 0. \qquad \forall w. \tag{A.2}$$

Using integration by parts

$$w \frac{\partial^2 p}{\partial x^2} = \frac{\partial}{\partial x}\left(w \frac{\partial p}{\partial x}\right) - \frac{\partial w}{\partial x}\frac{\partial p}{\partial x}, \tag{A.3}$$

Eq. (A.2) can be rewritten as

$$\int_0^L w \frac{\partial^2 p}{\partial t^2} dx - c^2 \left[\int_0^L \frac{\partial}{\partial x}\left(w \frac{\partial p}{\partial x}\right) dx - \int_0^L \frac{\partial w}{\partial x}\frac{\partial p}{\partial x} dx\right] = 0, \qquad \forall w, \tag{A.4}$$

which, using the fundamental theorem of calculus, can be simplified to

$$\int_0^L w \frac{\partial^2 p}{\partial t^2} dx - c^2 \left[w \frac{\partial p}{\partial x}\bigg|_\Gamma - \int_0^L \frac{\partial w}{\partial x}\frac{\partial p}{\partial x} \partial x\right] = 0, \qquad \forall w, \tag{A.5}$$

where Γ is the boundary of the 1D channel and consists of the two end points. In the following, the portion of the boundary where the p is prescribed is denoted by Γ_p, while the boundary where $\partial p/\partial x$ is prescribed is denoted by $\Gamma_{\partial p}$. Note that $\Gamma_p \cup \Gamma_{\partial p} = \Gamma$ and $\Gamma_p \cap \Gamma_{\partial p} = 0$. Next, we construct

the arbitrary function $w(x)$ so that $w = 0$ on Γ_p and the pressure field so that $p = \bar{p}$ on Γ_p, yielding

$$\int_0^L w \frac{\partial^2 p}{\partial t^2} dx - c^2 \left[w \frac{\partial p}{\partial x}\bigg|_{\Gamma_{\partial p}} - \int_0^L \frac{\partial w}{\partial x} \frac{\partial p}{\partial x} \partial x \right] = 0, \qquad \forall w \text{ with } w = 0 \text{ on } \Gamma_p, \tag{A.6}$$

To numerically solve Eq. (A.6), we then construct a mesh, introduce an approximation for the scalar fields p and w and formulate the discrete FE equations. Here, we discretize the 1D air channels into a number of line elements of length L_e and choose to approximate the fields in each line as a linear function (so that each element has two nodes located at x_1^e and x_2^e). It follows that over each element p and $\partial^2 p/\partial t^2$ are approximated as

$$p^e(x) = \mathbf{N}^e(x)\mathbf{d}^e, \qquad \frac{\partial^2 p^e(x)}{\partial t^2} = \mathbf{N}^e(x)\ddot{\mathbf{d}}^e, \tag{A.7}$$

where $\mathbf{d}^e$ and $\ddot{\mathbf{d}}^e$ are vectors containing the nodal values of p and $\partial^2 p/\partial t^2$ and

$$\mathbf{N}^e(x) = \frac{1}{L_e}[x_2^e - x,\ x - x_1^e] \tag{A.8}$$

is the so-called element shape function matrix. Note that the superscript e has been introduced to indicate that the functions pertain to element e. Moreover, according to the Galerkin method, we use the same approximation also for w,

$$w^e(x) = \mathbf{N}^e(x)\mathbf{w}^e. \tag{A.9}$$

Next, to efficiently integrate Eq. (A.6), we evaluate the integral over $[0,\ L]$ as a sum of integrals over individual element domains $[x_1^e,\ x_2^e]$,

$$\sum_{e=1}^{n_{el}} \left\{ \int_{x_1^e}^{x_2^e} w^{eT} \frac{\partial^2 p^e}{\partial t^2} dx + c^2 \int_{x_1^e}^{x_2^e} \frac{dw^{eT}}{dx} \frac{dp^e}{dx} dx - c^2 \left(w^{eT} \frac{dp^e}{dx} \right)_{\Gamma_{\partial p}^e} \right\} = 0, \tag{A.10}$$

where n_{el} is the total number of line element used to construct the mesh. Note that in the equation above we have taken the transpose of the arbitrary function w; this does not change the value of the expression as w is a scalar, but it is necessary for consistency when we substitute matrix expressions for w and its derivatives.

Substitution of Eqs. (A.7) and (A.9) into Eq. (A.10) yields

$$\sum_{e=1}^{n_{el}} \mathbf{w}^{eT} \left\{ \underbrace{\int_{x_1^e}^{x_2^e} \mathbf{N}^{eT}\mathbf{N}^e dx}_{\mathbf{M}^e} \ddot{\mathbf{d}}^e + \underbrace{c^2 \int_{x_1^e}^{x_2^e} \mathbf{B}^{eT}\mathbf{B}^e dx}_{\mathbf{K}^e} \mathbf{d}^e - \underbrace{c^2 \left(\mathbf{N}^{eT} \frac{dp}{dx} \right)_{\Gamma^e_{\partial p}}}_{\mathbf{f}^e} \right\} = 0, \tag{A.11}$$

where

$$\mathbf{B}^e = \frac{\partial \mathbf{N}^e}{\partial x} = \frac{1}{L_e}[-1,\ 1]. \tag{A.12}$$

Note that in Eq. (A.11) we have introduced the element matrices $\mathbf{M}^e$ and $\mathbf{K}^e$

$$\mathbf{M}^e = \int_{x_1^e}^{x_2^e} \mathbf{N}^{eT}\mathbf{N}^e dx = \frac{L_e}{6} \begin{bmatrix} 2 & 1 \\ 1 & 2 \end{bmatrix}, \qquad \mathbf{K}^e = c^2 \int_{x_1^e}^{x_2^e} \mathbf{B}^{eT}\mathbf{B}^e dx = \frac{c^2}{L_e} \begin{bmatrix} 1 & -1 \\ -1 & 1 \end{bmatrix}, \tag{A.13}$$

and the element vector $\mathbf{f}^e$

$$\mathbf{f}^e = c^2 \left(\mathbf{N}^{eT} \frac{dp}{dx} \right)_{\Gamma^e_{\partial p}}, \tag{A.14}$$

which are the essence of the FE method formulation for this problem and serve as the building block for its global implementation.

Since the element and global nodal vectors can be related as

$$\mathbf{d}^e = \mathbf{L}^e \mathbf{d}, \qquad \ddot{\mathbf{d}}^e = \mathbf{L}^e \ddot{\mathbf{d}}, \qquad \mathbf{w}^e = \mathbf{L}^e \mathbf{w}, \tag{A.15}$$

where $\mathbf{L}^e$ is the gather matrix for a given element, which gathers the nodel quantities of each element from the global nodal vector (note that $\mathbf{L}^e$ is a Boolean and consists strictly of ones and zeros). Substituting Eq. (A.15) into Eq. (A.11) we obtain

$$\mathbf{w}^T \left(\sum_{e=1}^{n_{el}} \mathbf{L}^{eT} \mathbf{M}^e \mathbf{L}^e \ddot{\mathbf{d}} + \sum_{e=1}^{n_{el}} \mathbf{L}^{eT} \mathbf{K}^e \mathbf{L}^e \mathbf{d} - \sum_{e=1}^{n_{el}} \mathbf{L}^{eT} \mathbf{f}^e \right) = 0. \tag{A.16}$$

If we now define the global matrices $\mathbf{M}$ and $\mathbf{K}$ as

$$\mathbf{M} = \sum_{e=1}^{n_{el}} \mathbf{L}^{eT} \mathbf{M}^e \mathbf{L}^e, \qquad \mathbf{K} = \sum_{e=1}^{n_{el}} \mathbf{L}^{eT} \mathbf{K}^e \mathbf{L}^e, \tag{A.17}$$

and the global vector $\mathbf{f}$ as

$$\mathbf{f} = \sum_{e=1}^{n_{el}} \mathbf{L}^{eT} \mathbf{f}^e, \tag{A.18}$$

Eq. (A.16) can be rewritten as

$$\mathbf{w}^T \left(\mathbf{M}\ddot{\mathbf{d}} + \mathbf{K}\mathbf{d} - \mathbf{f} \right) = 0. \tag{A.19}$$

Finally, since Eq. (A.19) has to be satisfied of all possible $\mathbf{w}$, it follows that

$$\mathbf{M}\ddot{\mathbf{d}} + \mathbf{K}\mathbf{d} - \mathbf{f} = 0, \tag{A.20}$$

which represent the FE equations for the 1D wave equation.

A.1.2 Frequency-domain analysis

To calculate the dispersion relation for an acoustic periodic network, we focus on its unit cell spanned by the lattice vectors $\mathbf{a}_1$ and $\mathbf{a}_2$ (highlighted in red in Fig. A.1). We then consider the wave motion

$$\mathbf{d} = \mathbf{p} e^{i\omega t}, \tag{A.21}$$

where $\mathbf{p}$ is the vector of nodal amplitudes of vibration and ω is the circular frequency. Introducing Eq. (A.21) into Eq. (A.20) we have

$$(\mathbf{K} - \omega^2\mathbf{M})\mathbf{p} = 0, \tag{A.22}$$

which is a generalized eigenvalue problem. Note that here we consider a unit cell in isolation from other unit cells, and thus the global vector $\mathbf{f}$ has been set to zero.

Next, we apply Bloch-type boundary conditions, so that the pressure of each pair of nodes (here denoted as A and B) periodically located on the boundary of the unit cell is related as

$$\mathbf{p}_B = \mathbf{p}_A \exp(i\mathbf{k} \cdot \mathbf{r}_{AB}), \tag{A.23}$$

where $\mathbf{k}$ is Bloch-wave vector and r_{AB} is the distance between the pair of nodes periodically located on the boundary.

Finally, we solve Eq. (A.22) with (A.23) for a number wave vectors $\mathbf{k}$ lying in the reciprocal space. Note that, since the reciprocal lattice is also periodic, we can restrict the wave vectors $\mathbf{k}$ to a certain region of the reciprocal space called the *first Brillioun zone* (indicated by the dashed polygons in Fig. A.1). In addition, we may further reduce the domain to the *irreducible Brillioun zone* (IBZ) (indicated by the yellow areas in Fig. A.1) by taking advantage of reflectional and rotational symmetries. Operationally, the band structures for the acoustic networks are constructed by calculating the eigen-frequencies $\omega(\mathbf{k})$ for $\mathbf{k}$ vectors on the perimeter of the IBZ and the band gaps (defined as frequencies range in which the propagation of the waves is forbidden) are obtained by the frequency ranges within no $\omega(\mathbf{k})$ exist. Numerically, a discrete set of $\mathbf{k}$ vectors on the perimeter of the IBZ needs to be chosen for the band gap calculations. For the simulations presented in this paper, twenty uniformly-spaced points on each edge of the IBZ are considered.

A.1.3 Dispersion relations for acoustic networks

While in Fig. 2.1 of Chapter 2 we report the dispersion relations for square and triangular lattices, we have also investigated the wave propagation in a number of other acoustic networks. In particular, in Fig. A.1 we report the dispersion relations for Kagome (see Fig. A.1(a)), hexagonal (see Fig. A.1(b)), equilateral pentagonal (see Fig. A.1(c)), mixed pentagons and rhombi (see Fig. A.1(d)) and snub square (see Fig. A.1(e)) configurations. Interestingly, the results indicate that any lattice comprising triangles or pentagons is characterized by frustration induced acoustic band gaps in the vicinity of the odd numbered resonance frequencies for the individual channels.

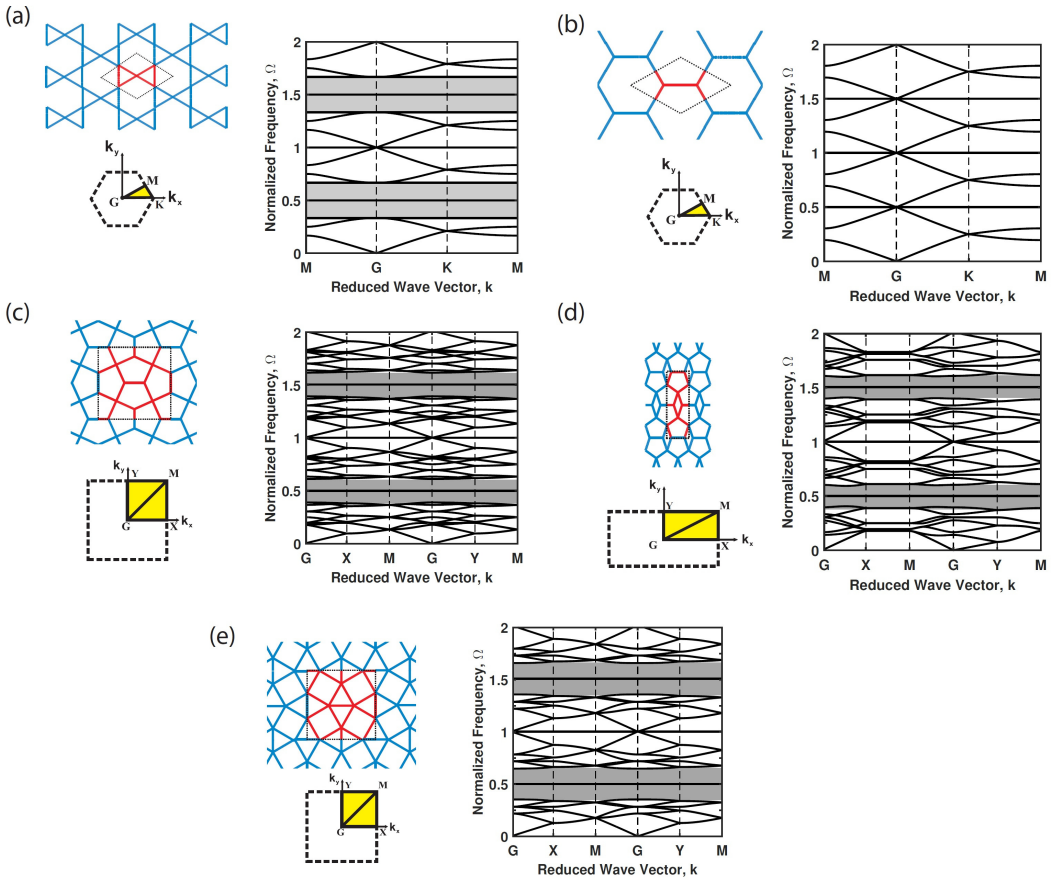

Figure A.1: Dispersion relations for acoustic networks comprising a periodic array of narrow air channels: (a) Kagome, (b) hexagonal, (c) equilateral pentagonal, (d) mixed pentagonal and rhombic, and (e) snub square lattices. Lattice configurations, unit cells (highlighted in red) and Brillioun zones are shown on the left. The calculated dispersion relations are shown on the right. The grey regions in the plots highlight the hybridization band gap induced by geometric frustration.

A.2 Effect of the finite width of the air channels

While the results presented in Fig. 2.1 of Chapter 2 are for ideal acoustic networks made of 1D channels, we have also investigated the effect of the finite width t of the tubes. To this end, we have performed FE simulations using the commercial package ABAQUS/Standard and studied the dynamic response of lattices comprising 2D rectangular channels of length L and width t meshed with 4-node bilinear acoustic elements (ABAQUS element type AC2D4). The calculated band structures for the square and triangular networks comprising comprising channels with different values of L/t are reported in Figs. A.2 and show that the dynamic response of the system is not significantly affected by the finite-width of the channels.

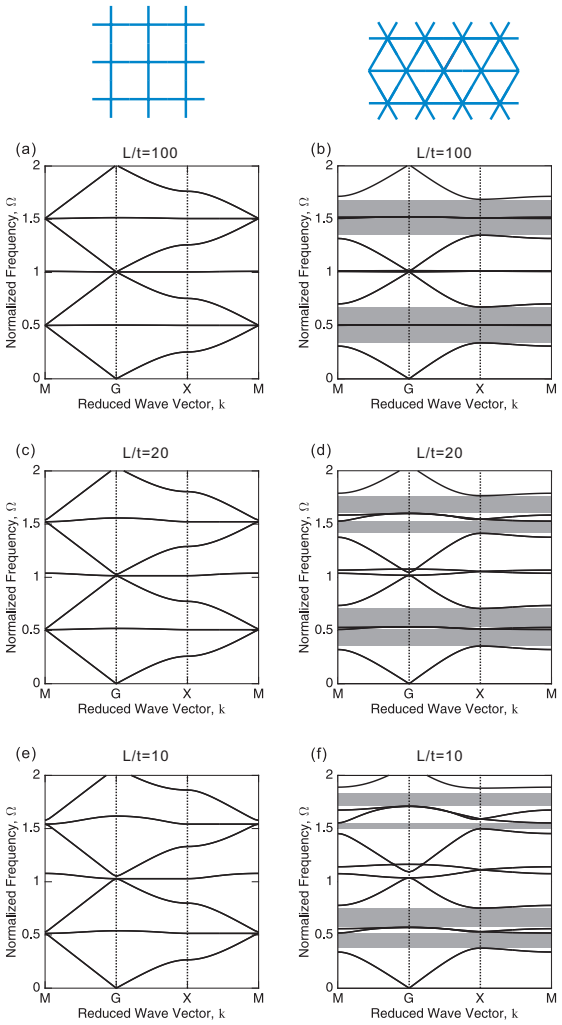

Figure A.2: Effect of the finite width of the channels: band structures for the square and triangular networks characterized by different values of L/t. The grey regions in the plots highlight the hybridization band gap induced by geometric frustration.

B

Supplemental Material to Chapter 3

B.1 Calculation of dispersion relations for beam lattices

B.1.1 Periodic lattices and unit cells

The propagation of elastic waves in beam lattices is investigated numerically by considering 2D periodic lattices of infinite extent and focusing on their unit cell (i.e. a repeating geometric unit). The unit cells used in this study are shown in Fig. B.1. Note that for hexagonal (Fig. B.1b) and rhombic

(Fig. B.1c) lattices, the unit cells used in the calculations are not the minimum repeating units. In both cases an enlarged rectangular unit cell is chosen to be able to investigate all topologically equivalent lattices (constructed by varying the angles between connected beams) using the same computational setup.

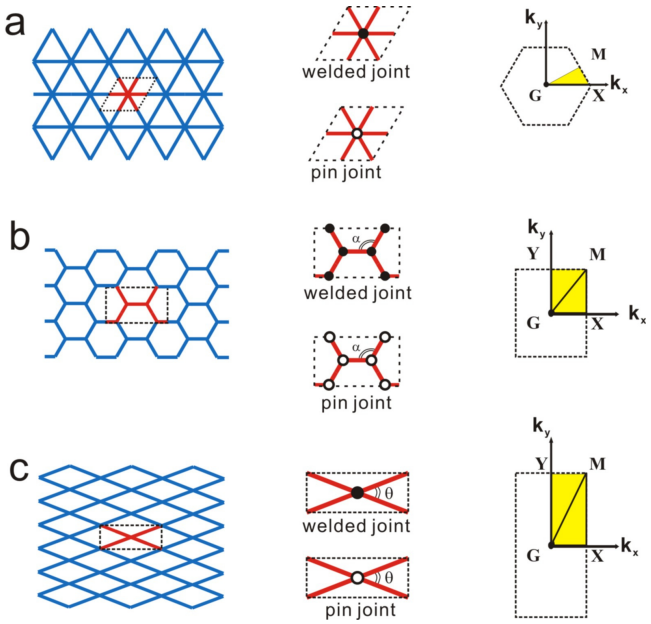

Figure B.1: Periodic lattices (left column) and their corresponding unit cells (central column), Brillioun zones (right column) and irreducible Brillioun zones (yellow shaded region) used in this study for: **a,** Triangular lattice; **b,** Hexagonal lattice and its topologically-equivalent variants; and **c,** Square lattice and its topologically-equivalent variants (rhombic lattices).

B.1.2 Frequency-domain analyses and Brillioun zones

In order to obtain the dispersion relations of the propagating waves in the periodic lattices, frequency domain analyses are performed via finite element (FE) simulations using the commercial software ABAQUS/STANDARD. Preliminary calculations were performed using using both Euler-Bernoulli beam elements (ABAQUS element type B23) and Timoshenko beam elements (ABAQUS element type B21). Since the two sets of simulations yielded identical results, we chose to use Euler-Bernoulli beam elements for all the simulations. Bloch-wave[4] boundary conditions are applied to the boundaries of the unit cells:

$$\mathbf{u}(\mathbf{x}+\mathbf{r}) = \mathbf{u}(\mathbf{x})e^{i\,\mathbf{k}\cdot\mathbf{r}}. \tag{B.1}$$

where $\mathbf{u}$, $\mathbf{x}$, $\mathbf{r}$ and $\mathbf{k}$ denote the degrees of freedom vector, position coordinates, spatial periodicity in the lattice configuration and bloch-wave vector, respectively. Note that for two-dimensional beam elements the vector $\mathbf{u}$ has three components, corresponding to two displacements (U1 and U2) and one rotation (UR3).

Focusing on the propagation of small-amplitude waves, we solve the linearized wave equation by using a perturbation method to obtain the dispersion relations $\omega = \omega(\mathbf{k})$. Due to the translational symmetry of the lattices, we only need to study $\omega(\mathbf{k})$ for $\mathbf{k}$ vectors in the *first Brillouin zone*[9,10]. Moreover, this domain can be further reduced by taking advantage of rotational, reflectional and inversional symmetries of the Brillouin zone. This allows us to define the *irreducible Brillouin zone* (IBZ)[71], shown as the yellow triangle $\mathbf{GXM}$ in Fig. B.1a and yellow rectangles $\mathbf{GXMY}$ in Figs. B.1b and B.1c. More details of mathematical formulation and numerical implementation are given in our previous publications[127,125].

The phononic bandgaps are identified by checking all eigen-frequencies $\omega(\mathbf{k})$ for $\mathbf{k}$ vectors on the perimeter of the IBZ. The bandgaps (i.e. range in frequencies for which the propagation of waves is

barred) are given by the frequency ranges within which no $\omega(\mathbf{k})$ exist. Numerically, a discrete set of $\mathbf{k}$ vectors on the IBZ perimeter needs to be chosen in the band-gap calculation. For the simulations presented in this paper, twenty uniformly-spaced points on each edge of the IBZ are used for the purpose of identifying band-gaps.

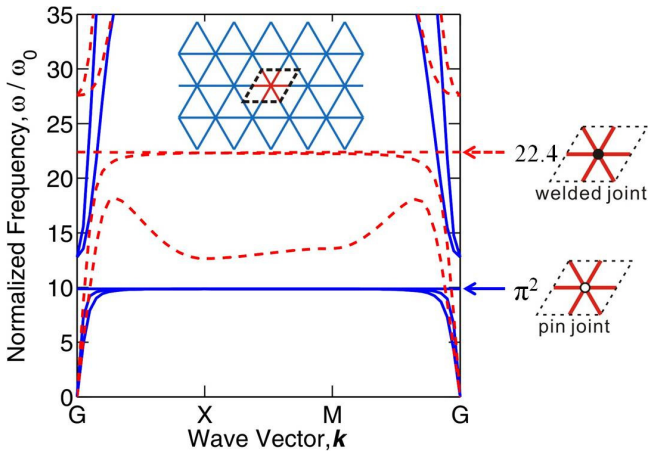

Figure B.2: Band structures of a triangular periodic beam lattices with welded (dashed red lines) and pin (continuous blue lines) joints. The frequency bands in the plot are normalized by $\omega_o = \omega_{pin}/\pi^2$.

B.2 Additional Results

B.2.1 Triangular lattice – comparison between pin and welded joints

The sound speed in the long-wavelength limit (i.e. the initial slope of the bands originated from **G**, the center of the *first Brillouin zone*) is directly correlated to the static homogenized stiffness of the structure. However, the slopes of the bands in Figs. 3.1a and 3.1b in Chapter 3 should not be compared directly for that purpose, since they are plotted using different normalization factors (i.e. the natural frequencies of a single beam with welded-welded and pin-pin boundary conditions,

respectively). In fact, ω_{welded} and ω_{pin} differ by a factor of $22.4/(3.14)^2 = 2.27$. To facilitate the direct comparison of the band structure reported in Figs. 1a and 1b, we normalized the band structure for the case of both welded and pin junctions using the same factor, $\omega_0 = \omega_{pin}/\pi^2 = \omega_{welded}/22.4$. These results are reported in Fig. B.2.

B.2.2 Hexagonal lattice and its topologically equivalent lattices with pin joints

In Chapter 3 we demonstrated that the dynamic response of the hexagonal lattice with welded joints is characterized by no locally resonant bandgap. Furthermore, we showed that no band gap exists in periodic lattices with welded joints that are still characterized by $\bar{z} = 3$, but for which the angle between connected beams, α, varies from $2\pi/3$ to $\pi/3$ (see Fig. 3.2 in Chapter 3).

Here, we report the band structures for the same lattices as those considered in Fig. 3.2 in Chapter 3, but with pin joints. The results shown in Fig. B.3 indicate that the flat-band resonant mode does not open a bandgap in this family of lattices even in the case of pin joints, confirming that the nature of the joints does not significantly affect the presence or absence of locally resonant bandgaps. However, it is important to note that the nature of the joints affects the static response of the system. In fact, the dispersion diagrams of the lattices with pin joints are characterized by a flat band at zero frequency [*] (indicated by the green lines in Fig. B.3). This flat band at $\omega = 0$ corresponds to a "floppy"[62,12,120,114,11] or "soft "[72,94] mode predicted by the Maxwell's Rule[75] and describes the *ground state* behavior of the lattice. Essentially, the existence of these zero-energy modes indicates that the lattice is not stable in a static sense and will collapse under infinitesimal perturbations. On the other hand, the full dispersion relation, including the "elevated flat bands" at $\omega/\omega_{pin} = 1$, defines the *excited state* response of the lattice under finite-energy dynamic loading. Interestingly, our results

[*] Note that such zero-frequency band is not present in the dispersion relation of a triangular lattice with pin joints (see Fig. 3.1b in Chapter 3), since in that case the network is stable according to Maxwell's Rule[75].

indicate that, differently from the ground state behavior, the excited state behavior of the lattices is not significantly affected by the nature of the joints.

Finally, it is worth noting that the band structures of a periodic lattices with $\bar{z} = 3$ and $\alpha = 2\pi/3$ (i.e. hexagonal lattice, see Fig. B.3a) and $\alpha = \pi/3$ (see Fig. B.3d) are identical. In fact, our numerical calculations show that for any β in the range $[0, \pi/2]$ the band structure of a periodic lattice with $\alpha = \pi/2 + \beta$ is the same as that of a lattice with $\alpha = \pi/2 - \beta$. More examples highlighting this symmetry are provided in Fig. B.4.

B.2.3 Periodic lattices with $3 \leq \bar{z} \leq 6$

To better understand the role of the coordination number on the formation of locally resonant bandgaps, we investigated the dynamic response of several periodic beam lattices with average connectivity $3 \leq \bar{z} \leq 6$ comprising an array of triangles and hexagons [†]. While in Fig. 3.3b in Chapter 3 we summarized the results by reporting the evolution of the width of the bandgap $\Delta\omega$ as a function of the coordination number $\bar{z}$, here we show the dispersion relations for some of these lattices.

We note that, in general, these hybrid lattices do not possess rotational, reflectional and inversional symmetries and that only the time reversal symmetry[48] is guaranteed, yielding:

$$\omega(\mathbf{k}) = \omega(-\mathbf{k}). \tag{B.2}$$

Therefore, Bloch vectors spanning half of the Brillouin zone need to be considered to construct the band structure. In practice, we calculate $\omega(\mathbf{k})$ for 21×21 different $\mathbf{k}$ vectors in half of the Brillouin zone and use the symmetry argument (Eq. (B.2)) to map the results to the other half.

In Figs. B.5, B.6 and B.7 we show the band structures for periodic lattices with $\bar{z} = 3.36$, $\bar{z} = 4.615$ and $\bar{z} = 5.143$, respectively. For $\bar{z} = 3.36$ no locally resonant bandgap is observed (see Fig. B.5). Differently, for $\bar{z} = 3.36$ both configurations with (see Fig. B.6-top) and without (see Fig. B.6-bottom) locally resonant bandgap are found. Finally, for the case of high average connectivity such as $\bar{z} = 5.143$ all considered lattices possess a locally resonant bandgap (see Fig. B.7).

[†]Note that the average connectivity can be easily calculated as the ratio between twice the total number of beams and the total number of nodes of the unit cell.

B.2.4 Rhombic lattices

In Chapter 3 we show that in rhombic lattices a locally resonant bandgap appears by progressively reducing the angle ϑ between the beams, regardless of the type of joints (see Fig. 3.4 in Chapter 3).

Here, we show the band structures for rhombic lattices with $\vartheta = \pi/18$ (see Fig. B.8-a), $\vartheta = \pi/6$ (see Fig. B.8-b), $\vartheta = \pi/3$ (see Fig. B.8-c) and $\vartheta = \pi/2$ (square lattice - see Fig. B.8-d). Both lattices with welded and pin joints are considered. Note that for the cases of pin joints the lattices are characterized by a zero-frequency mode in the $\mathbf{G} - \mathbf{M}$ direction (see green lines in Fig. B.8), since the structures are isostatic and can be infinitesimally deformed without incurring any energy cost.

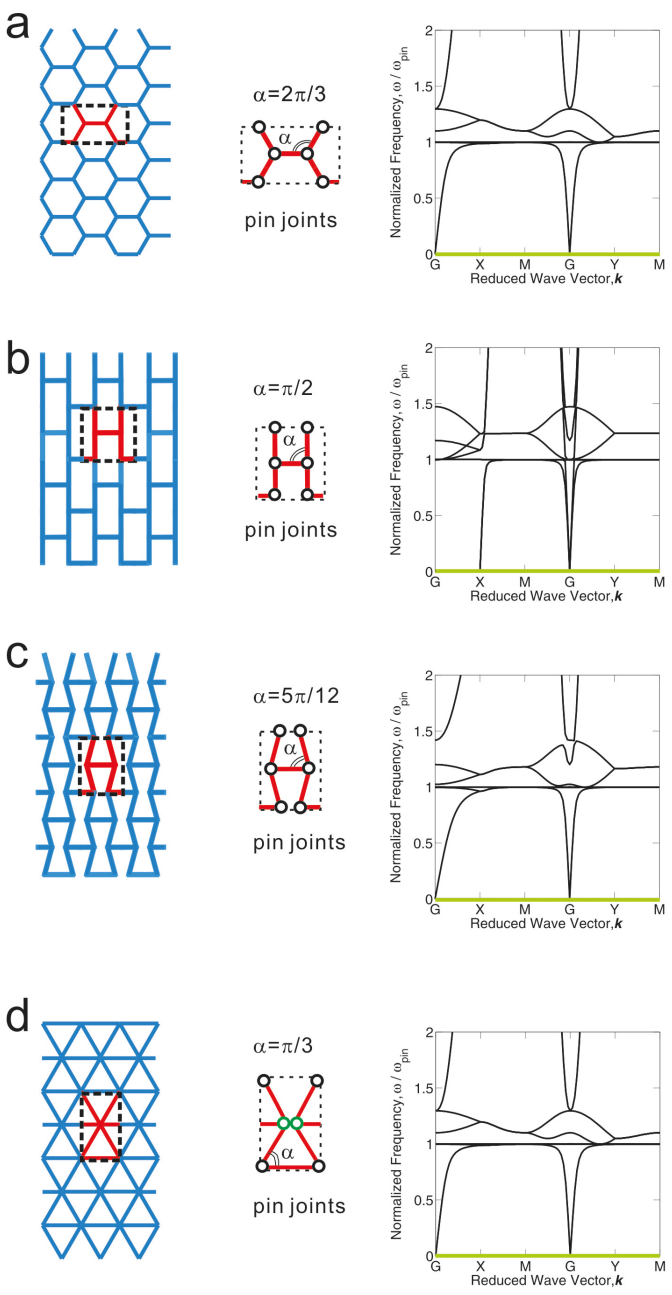

Figure B.3: Band structures of periodic lattices with $\bar{z} = 3$ and pin joints. The lattice structures and unit cells used in the calculations are shown on the left. **a,** Hexagonal lattice ($\alpha = 2\pi/3$); **b,** Topologically equivalent lattice with $\alpha = \pi/2$; **c,** Topologically equivalent lattice with $\alpha = 5\pi/12$; and **d,** Topologically equivalent with $\alpha = \pi/3$. Note that the arrangement of the beams in **d** is the same as in the triangular lattice, but the connectivity is still $\bar{z} = 3$. In fact, although for clarity the green-colored joints are drawn separately in the unit cell of **d**, they are positioned at the same spatial location. No locally resonant bandgap is found for any of the configurations. The zero-frequency floppy modes are highlighted as green lines. Results for the same lattices with welded joints are provided in Chapter 3.

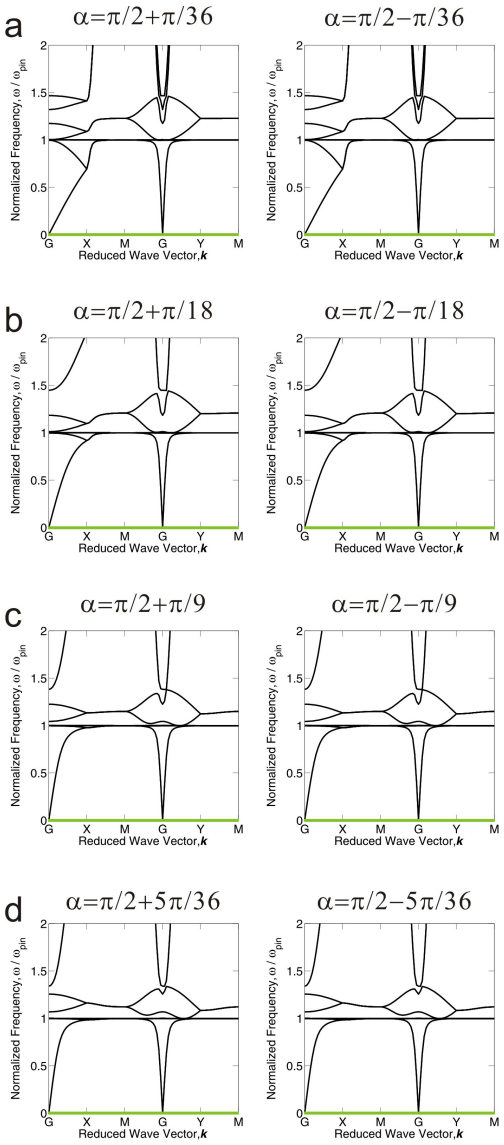

Figure B.4: Symmetry in the band structures of periodic lattices with $\bar{z} = 3$ and pin joints. All results are for pin-jointed lattices that are topologically equivalent to the hexagonal lattice. Each row shows the dispersion relations for lattices with $\alpha = \pi/2 + \beta$ (left column) and $\alpha = \pi/2 - \beta$ (right column). In particular, we report results for with **a,** $\beta = \pi/36$; **b,** $\beta = \pi/18$; **c,** $\beta = \pi/9$; and **d,** $\beta = 5\pi/36$. The zero-frequency floppy modes are highlighted as green lines.

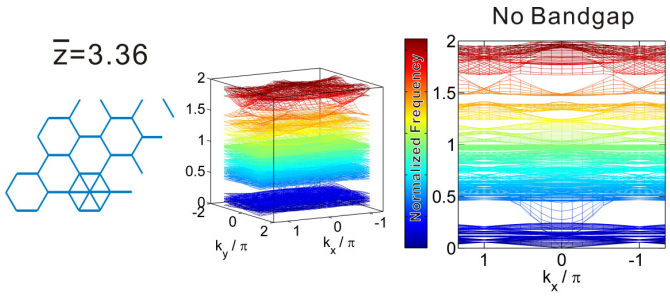

Figure B.5: Band structure for a periodic lattice with average connectivity $\bar{z} = 3.36$.

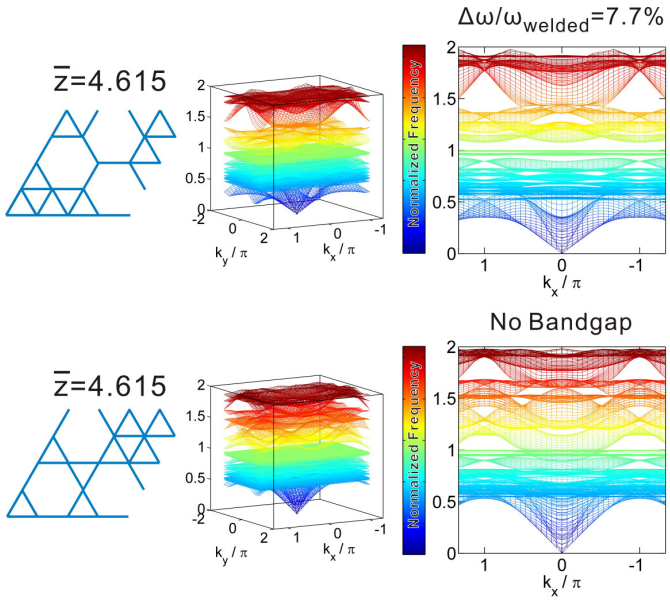

Figure B.6: Band structures for periodic lattices with average connectivity $\bar{z} = 4.615$.

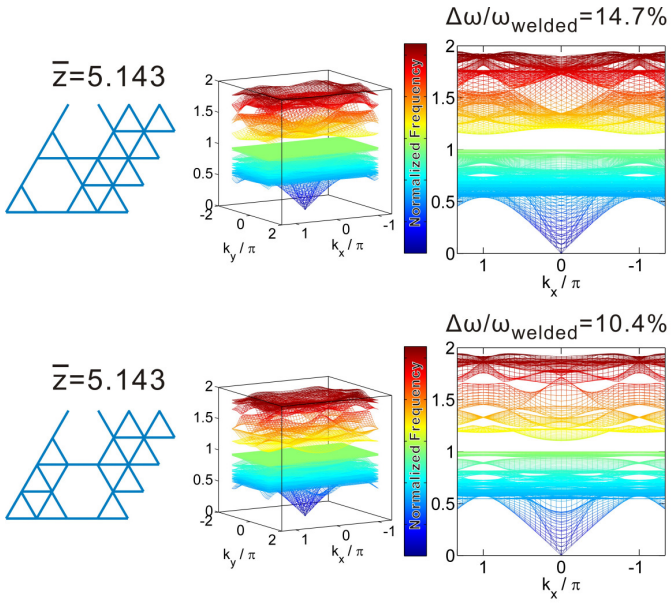

Figure B.7: Band structures for periodic lattices with average connectivity $\bar{z} = 5.143$.

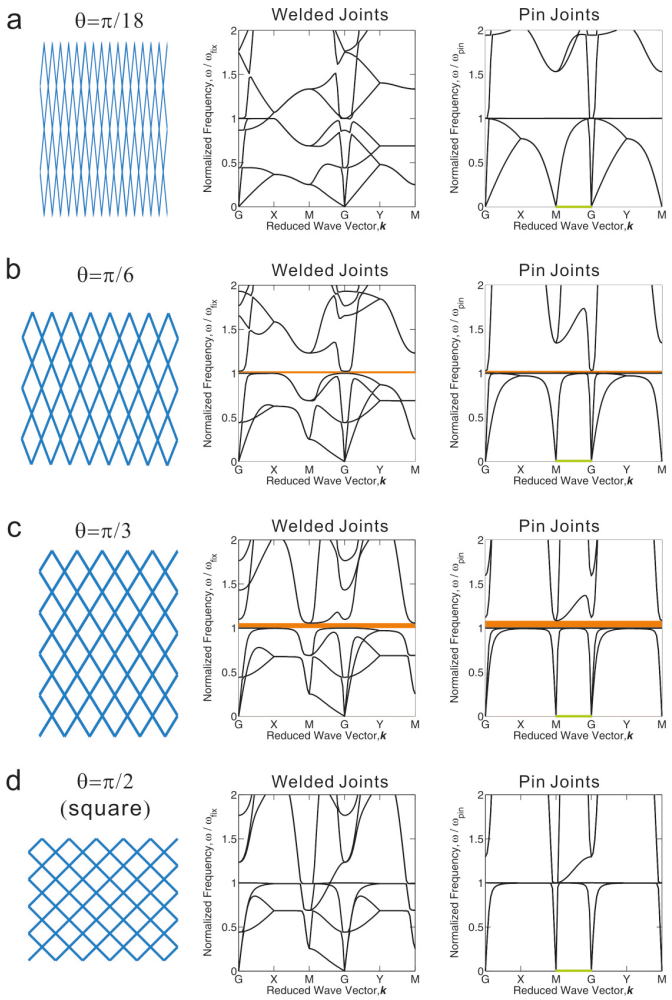

Figure B.8: Dispersion relations of rhombic lattices ($\bar{z} = 4$) with welded and pin joints. The zero-frequency floppy modes in the **G-M** direction are highlighted as green lines. The bandgaps are highlighted as orange color-shaded area. **a,** $\vartheta = \pi/18$; **b,** $\vartheta = \pi/6$; **c,** $\vartheta = \pi/3$; and **d,** $\vartheta = \pi/2$ (square lattice)

C

Supplemental Material to Chapter 4

C.1 Polarization characteristics

By calculating the dispersion relation for the lattices considered in this study, four Bloch modes (corresponding to four bands) for each $\mathbf{k}$ vector are obtained. Each Bloch mode takes the vector form

$\mathbf{U} = [u_x^{m_1},\ u_y^{m_1},\ u_x^{m_2},\ u_y^{m_2}]$, whose components are complex numbers:

$$U_1 = u_x^{m_1} = u_{x,re}^{m_1} + iu_{x,im}^{m_1}, \tag{C.1}$$

$$U_2 = u_y^{m_1} = u_{y,re}^{m_1} + iu_{y,im}^{m_1}, \tag{C.2}$$

$$U_3 = u_x^{m_2} = u_{x,re}^{m_2} + iu_{x,im}^{m_2}, \tag{C.3}$$

$$U_4 = u_y^{m_2} = u_{y,re}^{m_2} + iu_{y,im}^{m_2}. \tag{C.4}$$

$$\tag{C.5}$$

The full expression of each vibrational mode in real space is then given by

$$\tilde{\mathbf{U}} = Re[\mathbf{U} \exp{(i\mathbf{k}\cdot\mathbf{r} - i\omega t)}], \tag{C.6}$$

whose components can be rewritten as

$$\tilde{U}_j = Re[U_j]\ \cos(\Omega) - Im[U_j]\ \sin(\Omega) = \mathcal{A}_j \cos(\Omega + B_j), \quad \text{for}\, j = 1, .., 4 \tag{C.7}$$

where $\Omega = \mathbf{k}\cdot\mathbf{r} - \omega t$ and the j-th components of the amplitude vector $\mathbf{A}$ and phase vector $\mathbf{B}$ are defined as

$$\mathcal{A}_j = \sqrt{Re[U_j]^2 + Im[U_j]^2}, \quad B_j = \arctan\left[\frac{Im[U_j]}{Re[U_j]}\right]. \tag{C.8}$$

To better understand the polarization of the modes for the ordinary (non-gyroscopic) and gyroscopic hexagonal lattices, in Figs. C.1 and C.2 we plot the model displacement trajectories of m_1 and m_2 by varying Ω in Eqn. (C.7) from 0 to 2π. Note that all the amplitudes have been normalized by $\max_{j=1,2,3,4}(\mathcal{A}_j)$.

In particular, in Fig. C.1 we focus on the ordinary hexagonal lattice. As expected, in the long wavelength regime (near G-point) all four bands are linearly polarized. The first and forth bands

correspond to transverse modes, while the second and third bands are longitudinal modes. Differently, for short wavelengths (near K-points) all modes are found to have mixed polarization. Note that in the Figure we report the modal polarization for four different wave vectors (G_K, K_1, K_2 and K) pointing in the same (horizontal) direction, but with different wavelengths (as indicated in the Brillouin zone on the top of the Figure). The results indicate a gradual transition from linearly polarized modes to modes with mixed polarization as the wavelength decreases.

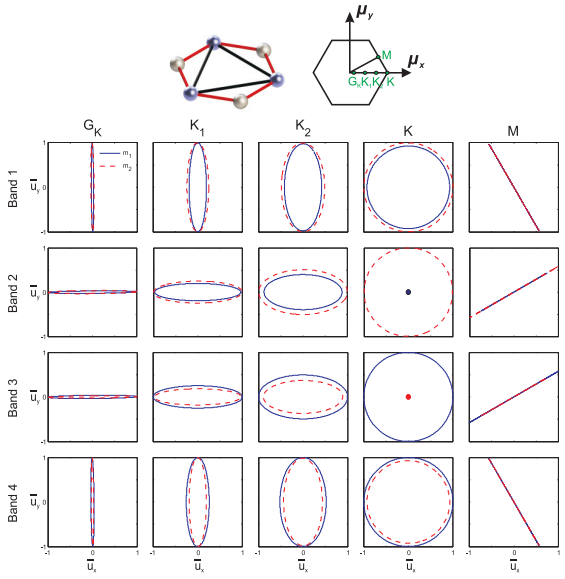

Figure C.1: Modal polarization for the ordinary hexagonal lattice (i.e. $\alpha_1 = \alpha_2 = 0$): Note that blue solid lines indicate polarization of m_1, while the red dashed lines represent the polarization of m_2. Results are reported for four $\mathbf{k}$-space points on the G-K line and the M point, as indicated in the Brillouin zone on the top of the figure.

In Fig. C.2 we then report the modal displacement trajectories for the gyroscopic hexagonal lattice. By comparing the modal polarizations of the non-gyroscopic (Fig. C.1) and gyroscopic (Fig. C.2) hexagonal lattices, we can clearly see that a band inversion between the 2nd and 3rd bands occurs at K-points, indicating a topological transition. Furthermore, the modal mixing of the transverse and longitudinal polarizations for the 3rd and 4th bands near the G-point (at the G_K-point) also clearly indicates a topological transition occurring at the center of the Brillouin zone.

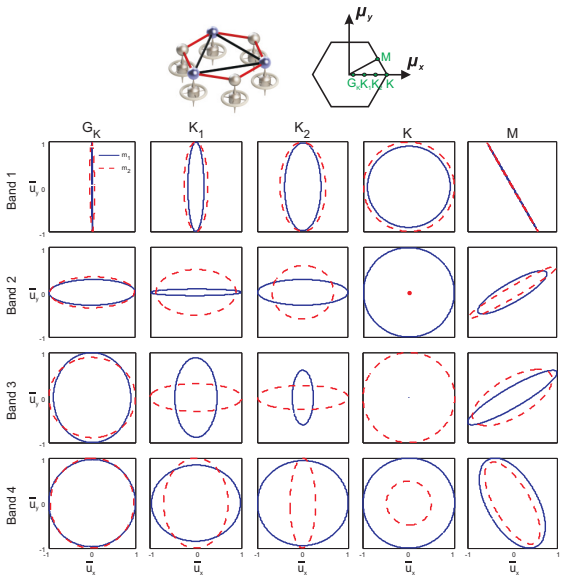

Figure C.2: Modal polarization for the gyroscopic hexagonal lattice with $\alpha_1 = \alpha_2 = 0.3m_1$: Note that blue solid lines indicate polarization of m_1, while the red dashed lines represent the polarization of m_2. Results are reported for four $\mathbf{k}$-space points on the G-K line and the M point, as indicated in the Brillouin zone on the top of the figure.

C.2 Band inversion in gyroscopic hexagonal lattices

In Fig. C.3 we report the evolution of the band structure for the gyroscopic hexagonal lattice considered in Chapter 4. The band structures show that for $\alpha = \alpha_1 = \alpha_2 > 0$, a new topologically non-trivial gap between the 3rd and 4th bands is opened by lifting the quadratic degeneracy at *G*-point (the center of the Brillouin zone). Furthermore, we see that the size of this gap increases monotonically with α.

Differently, the gap observed in the ordinary (non-gyroscopic) lattice between the 2nd and 3rd bands initially gets narrower for increasing values of α. It eventually closes at $\alpha = 0.07 m_1$, where a pair of Dirac-like linear crossing cones in the first Brillouin zone emerges. Note that there are six *K*-points due to six fold symmetry in the wave vector μ-space, but only one third of the cone at each *K*-point is included in the first Brillouin zone. Finally, for $\alpha > 0.07 m_1$ a new (topologically non-trivial) gap is opened by lifting the pair of Dirac-like cones, so that the system is characterized by two topologically non-trivial gaps.

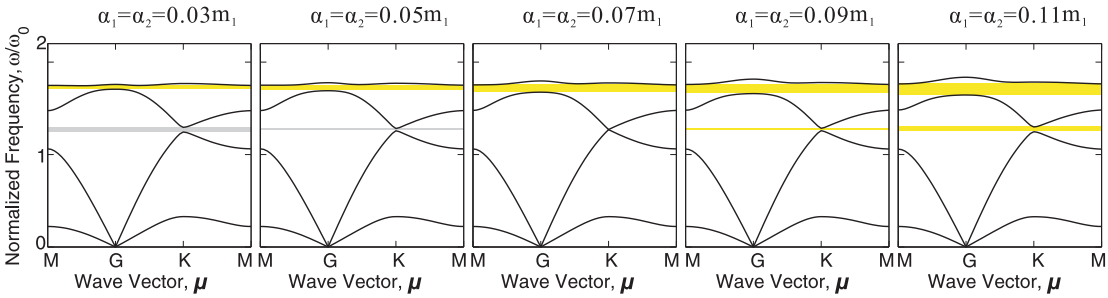

Figure C.3: Evolution of the band structure for the gyroscopic hexagonal lattice as a function of α: Note that the grey and yellow shaded areas highlight topologically trivial and non-trivial gaps, respectively.

Importantly, we also find that the topological transition is accompanied by a local band inversion near *K*-points. In fact, the results shown in Fig. C.4 for the modal polarizations of m_1 and m_2 at

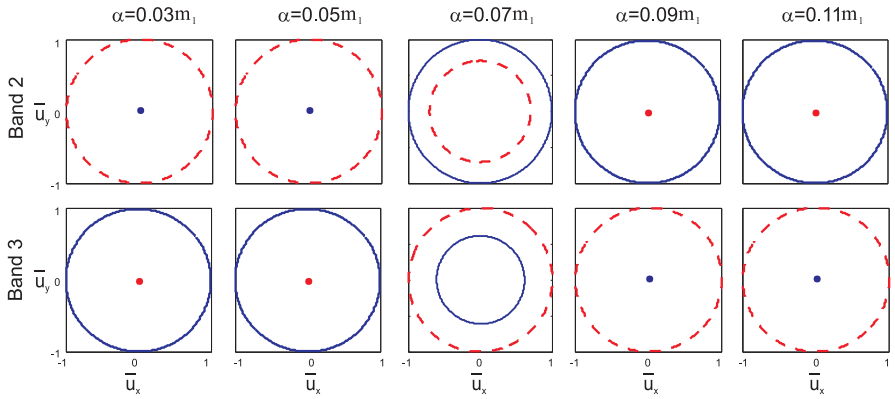

Figure C.4: Band inversion process during symmetry breaking demonstrated by the evolution of the modal polarizations of 2nd and 3rd bands at K-points as a function of α

K-points reveal that a local mode switching between the 2nd and 3rd bands occurs during the topological transition at $\alpha = 0.07m_1$. For $\alpha < 0.07m_1$ we find that the motion of m_2 dominates for the second band, while the motion of m_1 dominates for the third band. A switch occur at $\alpha = 0.07m_1$, so that when $\alpha > 0.07m_1$ we find that the motion of m_1 dominates for the second band, while the motion of m_2 dominates for the third band. We note that similar band inversion during topological phase change has recently been experimentally observed in one-dimensional acoustic systems[137].

C.3 Topological phase diagram

To better understand the process resulting in the formation of the topologically non-trivial gap between the 2nd and the 3rd bands, we also investigate the effect of symmetry breaking for spatial inversion (P) and time reversion (T). As shown in Fig. C.5a, for a non-gyroscopic lattice with both P-T symmetries no gap is observed. Moreover, a Dirac-like crossing pair is found at the K point between the 2nd and the 3rd bands. When the time-reversal symmetry is broken by adding gyroscopes (Fig. C.5b) the Dirac-like crossing pair is lifted and a topologically non-trivial gap forms (highlighted by the yellow shaded area in Fig. C.5b).

On the other hand, when only the P-symmetry is broken by removing three black springs in the non-gyroscopic lattice (as shown in Fig. C.5c), the Dirac-like crossing pair is also lifted, but the emerging gap (highlighted by the grey shaded area in Fig. C.5c) is topologically trivial. Next, when also the T symmetry is broken by adding gyroscopes (Figs. C.5d and e), we find that the band structure strongly depends on the relative strength of P-breaking and T-breaking. When P-breaking is dominant, only topologically trivial gaps are found. By contrast, when T-breaking is dominant, topologically non-trivial gaps form. Finally, we note that when P-breaking and T-breaking are balanced (as in Fig. C.5d) a Dirac-like crossing pair forms at the K point closing the band gap.

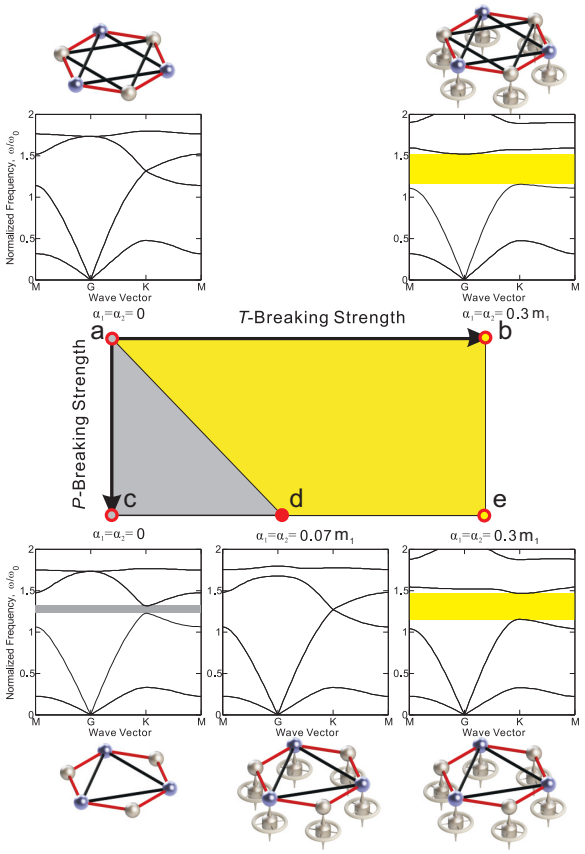

Figure C.5: Topological phase diagram of the hexagonal phononic crystal. **(a)** Phononic crystal with both P and T symmetries. The Dirac-like cones connecting the 2nd and 3rd bands at the K-point are protected by the PT symmetry. No gap is formed. **(b)** Topologically non-trivial gap emerges between the 2nd and 3rd bands due to broken T symmetry. **(c)** Topologically trivial gap emerges between the 2nd and 3rd bands due to broken P symmetry. **(d)** When P symmetry breaking and T symmetry breaking are balanced, the Dirac-like cones persist. **(e)** When the T symmetry breaking strength dominates the T symmetry breaking strength, the Dirac-like cones are lifted to form a topologically non-trivial gap

C.4 Additional results for square lattice

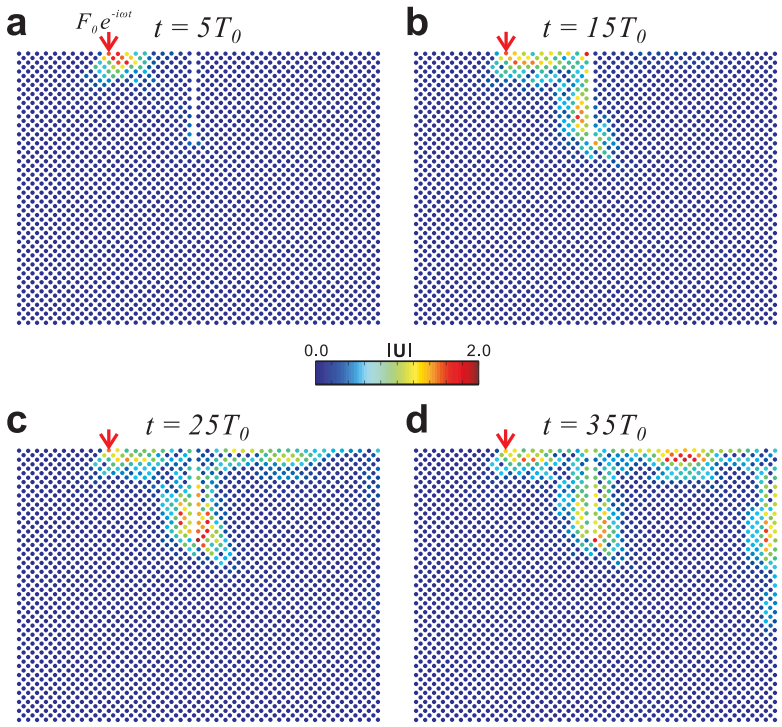

Figure C.6: Transient Response of a gyroscopic phononic crystal consisting of 40×30 square unit cells with a line defect on the top boundary: Snapshots of the velocity field at **(a)** $t = 5T_0$, **(b)** $t = 15T_0$, **(c)** $t = 25T_0$ and **(d)** $t = 35T_0$, where $T_0 = \sqrt{m_1/k_1}$ is the characteristic time scale of the system. Starting from $t = 0$, a time-harmonic excitation force $\mathbf{F}(t) = [F_x(t),\ F_y(t)] = [1,\ 1]F_0 e^{-i\omega t}$ is prescribed at the site indicated by the red arrow.

C.5 Formulation of gyroscope

The gyroscope considered in this study has its top tip of the rotational axis pinned to a concentrated mass site in the phononic crystal, and the bottom tip pinned to the ground (Fig. C.7). Because of this any translational motion is prevented, while they can free rotate. Each gyroscope has 3 degrees of freedom described by the spin (ψ), precession (φ) and nutation (ϑ) angles with respect to the vertical z-axis, as shown in Fig. C.7. Assuming constant spin and precession rates ($\dot{\psi} = \Psi$, $\dot{\varphi} = \Phi$ and $\ddot{\psi} = \ddot{\varphi} = 0$), its equations of motion can be written as [37,14,17]:

$$\mathcal{M}_x = I_{xx}(\ddot{\vartheta} - \Phi^2 \sin\vartheta\cos\vartheta) + I_{zz}\Phi\sin\vartheta(\Phi\cos\vartheta + \Psi) \tag{C.9}$$

$$\mathcal{M}_y = (2I_{yy}\Phi\dot{\vartheta}\cos\vartheta) - I_{zz}\dot{\vartheta}(\Phi\cos\vartheta + \Psi))\sin\vartheta \tag{C.10}$$

$$\mathcal{M}_z = I_{zz}\Phi\dot{\vartheta}\sin\vartheta \tag{C.11}$$

where $\mathcal{M}_x$, $\mathcal{M}_y$ and $\mathcal{M}_z$ are moments about the x, y and z axes, respectively, and I_{xx}, I_{yy} and I_{zz} are the second moments of inertia. Note that in the absence of external moments $\mathcal{M}_x = \mathcal{M}_y = 0$ and that for symmetric gyroscopes (as those considered in this study) $I_{xx} = I_{yy} = I_0$.

Here we consider a small amplitude time-harmonic in-plane motion at the top tip of the gyroscope induced by the lattice vibration,

$$U_{tip} = h\sin(\vartheta) \approx h\vartheta = h\Theta e^{i\omega t} \qquad \text{for} \quad |\Theta| \ll 1, \tag{C.12}$$

where h is the height of the gyroscope. Under such assumption of small amplitude tip displacement ($\sin\vartheta \approx \vartheta$ and $\cos\vartheta \approx 1$), Eqn. (C.10) can then be simplified to provide the relation between

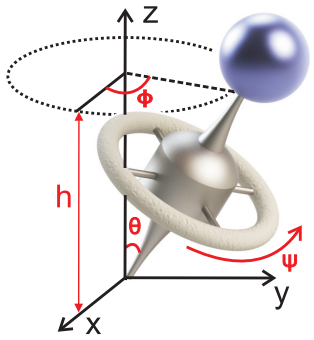

Figure C.7: Gyroscope: Schematic of a gyroscope with the top tip pinned to a mass in the lattice.

precession rate and spin rate,

$$\dot{\varphi} = \Phi = \left(\frac{I_{zz}}{2I_0 - I_{zz}}\right)\Psi \tag{C.13}$$

Moreover, substitution of Eqn. (C.12) into Eqn. (C.9) yields,

$$(I_{zz} - I_0)\Phi^2 + I_{zz}\Psi\Phi - I_0\omega^2 = 0 \tag{C.14}$$

which can be combined with Eqn. (C.13) to give

$$\Psi = \pm\omega\frac{2I_0 - I_{zz}}{I_{zz}} \tag{C.15}$$

Note that, for $\omega = 0$, then $\Psi = 0$ implies that the gyroscope is not spinning and there is no rotational inertial coupling effect.

Finally, introducing Eqn. (C.15) into Eqn. (C.11), we arrive at

$$\mathcal{M}_z = \pm\omega\dot{\vartheta}\vartheta I_{zz} = \pm i\omega^2\vartheta^2 I_{zz} \tag{C.16}$$

Next, we determine the gyroscopic force F_g between the gyroscope and the concentrated mass pinned at its top. F_g is perpendicular to the direction of U_{tip} in the xy-plane and has to satisfy the

balance of moment about the z-axis:

$$\mathcal{M}_z = F_g h \sin\vartheta \approx F_g h \vartheta \tag{C.17}$$

Combining Eqns. (C.16) and (C.17), we finally conclude that F_g takes the form

$$F_g = \pm i \frac{\omega^2}{h^2} I_{zz} U_{tip} \tag{C.18}$$

Therefore, when the mass connected at the top tip of the gyroscope is displaced by $\mathbf{U}_{tip} = [u_x, u_y]$, the effective gyroscopic inertial force is given as:

$$\mathbf{F}_g = \pm i \frac{\omega^2}{h^2} I_{zz} \mathbf{R} \mathbf{U}_{tip}, \tag{C.19}$$

where $\mathbf{R}$ is the rotation matrix,

$$\mathbf{R} = \begin{pmatrix} 0 & 1 \\ -1 & 0 \end{pmatrix} \tag{C.20}$$

introduced to make the direction of $\mathbf{F}_g$ orthogonal to $\mathbf{U}_{tip}$.

Consequently, to take this rotational inertial effect into account, the mass matrix associated to each mass is given by

$$\tilde{\mathbf{M}} = \begin{pmatrix} m & i\alpha \\ -i\alpha & m \end{pmatrix}, \tag{C.21}$$

where $\alpha = \pm I_{zz}/h^2$ represents the inertia coupling with a phase shift dictated by the imaginary multiplier i. This imaginary nature of the gyroscopic inertial effect indicates directional phase shifts between two independent directions of the tip displacements, which breaks time-reversal symmetry[123].

C.6 Calculation of Chern numbers

We start by noting that the frequency-domain wave equation for a lattice is given by

$$\mathbf{K}(\mu)\mathbf{U} = \omega^2\tilde{\mathbf{M}}\mathbf{U}, \tag{C.22}$$

where μ is the Bloch-wave vector.

Solving Eqn. (C.22) on the unit cell for wave vectors μ within the first Brillouin zone, we obtain the dispersion relation $\omega = \omega(\mu)$ (eigenvalue) and the associated modal displacement vector field $\mathbf{U}(\mu)$ (eigenvector).

For a two-dimensional (2D) lattice, we use a $N_{\mu_1} \times N_{\mu_2}$ grid that covers the first Brillouin zone in the 2D μ-space. The modal displacement associated to the n-th band is then a vector field, $\mathbf{U}_n(\mu) = \mathbf{U}_n(\mu_1, \mu_2)$ defined on a 2D discretized parametric domain.

In the following we focus on modal displacement associated to the n-th band (for the sake of simplicity, we drop the subscript n) and define the modal inner product as follows:

$$\langle \mathbf{U}(\mu)|\mathbf{U}(\mu')\rangle = \mathbf{U}(\mu)\cdot\tilde{\mathbf{M}}\mathbf{U}(\mu') = \sum\nolimits_{p,q} U_p^*(\mu)\tilde{M}_{pq}U_q(\mu') \tag{C.23}$$

where U_p and U_q are components of vector $\mathbf{U}$, and $(\cdot)^*$ denotes the operation of complex conjugation.

Following an approach that is conceptually similar to the method proposed in [35], we calculate the Berry flux, $\tilde{F}_{12}$, for a small patch of the size $\Delta\mu_1 \times \Delta\mu_2$ on the μ-grid:

$$\tilde{F}_{12}(\mu) = \ln\left(\frac{\langle \mathbf{U}(\mu)|\mathbf{U}(\mu')\rangle \langle \mathbf{U}(\mu')|\mathbf{U}(\mu'')\rangle \langle \mathbf{U}(\mu'')|\mathbf{U}(\mu''')\rangle \langle \mathbf{U}(\mu''')|\mathbf{U}(\mu)\rangle}{\langle \mathbf{U}(\mu)|\mathbf{U}(\mu)\rangle \langle \mathbf{U}(\mu')|\mathbf{U}(\mu')\rangle \langle \mathbf{U}(\mu'')|\mathbf{U}(\mu'')\rangle \langle \mathbf{U}(\mu''')|\mathbf{U}(\mu''')\rangle}\right), \tag{C.24}$$

where $\mu = (\mu_1, \mu_2)$, $\mu' = (\mu_1 + \Delta\mu_1, \mu_2)$, $\mu'' = (\mu_1 + \Delta\mu_1, \mu_2 + \Delta\mu_2)$ and $\mu''' = (\mu_1, \mu_2 + \Delta\mu_2)$.

Here $\tilde{F}_{12}$ is defined within the principal branch of the logarithm function, such that

$$-\pi < \frac{1}{i}\tilde{F}_{12}(\mu_1, \mu_2) \leq \pi \qquad \forall \mu_1, \mu_2 \quad . \tag{C.25}$$

As shown in Ref.[35], we note that the denominator in Eqn. (C.24) cannot vanish in order for it to be well defined. This condition can always be satisfied by a infinitesimal shift of the $N_{\mu_1} \times N_{\mu_2}$ grid in μ-space.

Finally, the numerical Chern number can be calculated by integrating the Berry flux over the entire first Brillouin zone:

$$C = \frac{1}{2\pi i} \sum_{\mu_1} \sum_{\mu_2} \tilde{F}_{12}(\mu_1, \mu_2). \tag{C.26}$$

In addition, we note that when two or more bands share degenerate point(s) in band structure (e.g. the first and second bands always have a degeneracy at $\omega \to 0$), their combined Chern number should be calculated instead of individual ones.

To get the combined Chern number for the n-th and m-th bands, for instance, all four inner products of the form $\langle \mathbf{U}(\mu) | \mathbf{U}(\mu') \rangle$ in the numerator of Eq. (C.24) need to be replaced by the *determinant* of a 2×2 matrix $\mathbf{P}(\mu, \mu')$:

$$\mathbf{P}(\mu, \mu') = \begin{pmatrix} \langle \mathbf{U}_n(\mu) | \mathbf{U}_n(\mu') \rangle & \langle \mathbf{U}_n(\mu) | \mathbf{U}_m(\mu') \rangle \\ \langle \mathbf{U}_m(\mu) | \mathbf{U}_n(\mu') \rangle & \langle \mathbf{U}_m(\mu) | \mathbf{U}_m(\mu') \rangle \end{pmatrix}, \tag{C.27}$$

If three or more bands are crossing each other, the matrix $\mathbf{P}(\mu, \mu')$ defined in Eq. (C.27) can be easily generalized to a 3×3 or higher order matrix.

Bibliography

[1] Alexander, S. (1998). Amorphous solids: their structure, lattice dynamics and elasticity. *Physics Reports*, 296(2¨C4), 65 – 236.

[2] Balents, L. (2010). Spin liquids in frustrated magnets. *Nature*, 464(7286), 199–208.

[3] Bigoni, D., Guenneau, S., Movchan, A. B., & Brun, M. (2013). Elastic metamaterials with inertial locally resonant structures: Application to lensing and localization. *Physical Review B*, 87, 174303.

[4] Bloch, F. (1929). Über die quantenmechanik der elektronen in kristallgittern. *Zeitschrift für physik*, 52(7-8), 555–600.

[5] Boechler, N., Eliason, J. K., Kumar, A., Maznev, A. A., Nelson, K. A., & Fang, N. (2013). Interaction of a contact resonance of microspheres with surface acoustic waves. *Physical Review Letters*, 111, 036103.

[6] Boechler, N., Wallen, S., Ghanem, M. A., Jenks, J., & Vogel, N. (2015). A self-assembled metamaterial for lamb waves. *Physical Review Letters*, 107, 071903.

[7] Bramwell, S. T. & Gingras, M. J. (2001). Spin ice state in frustrated magnetic pyrochlore materials. *Science*, 294(5546), 1495–1501.

[8] Branford, W., Ladak, S., Read, D., Zeissler, K., & Cohen, L. (2012). Emerging chirality in artificial spin ice. *Science*, 335(6076), 1597–1600.

[9] Brillouin, L. (1946). *Wave Propagation in Periodic Structures*. McGraw-Hill.

[10] Brillouin, L. (1960). *Wave Propagation and Group Velocity*. Academic Press.

[11] Broedersz, C. P. & MacKintosh, F. C. (2014). Modeling semiflexible polymer networks. *Reviews of Modern Physics*, 86, 995.

[12] Broedersz, C. P., Mao, X., Lubensky, T. C., & MacKintosh, F. C. (2011). Criticality and isostaticity in fibre networks. *Nature Physics*, 7, 983.

[13] Brûlé, S., Javelaud, E. H., Enoch, S., & Guenneau, S. (2014). Experiments on seismic metamaterials: Molding surface waves. *Physical Review Letters*, 112, 133901.

[14] Brun, M., Jones, I. S., & Movchan, A. B. (2012). Vortex-type elastic structured media and dynamic shielding. *Proceedings of the Royal Society of London A: Mathematical, Physical and Engineering Sciences*, 468(2146), 3027–3046.

[15] Bryngelson, J. D. & Wolynes, P. G. (1987). Spin glasses and the statistical mechanics of protein folding. *Proceedings of the National Academy of Sciences*, 84(21), 7524–7528.

[16] Calladine, C. (1978). Buckminster fuller's ¡°tensegrity¡± structures and clerk maxwell's rules for the construction of stiff frames. *International Journal of Solids and Structures*, 14(2), 161 – 172.

[17] Carta, G., Brun, M., Movchan, A., Movchan, N., & Jones, I. (2014). Dispersion properties of vortex-type monatomic lattices. *International Journal of Solids and Structures*, 51(11), 2213–2225.

[18] Casadei, F., Beck, B., Cunefare, K. A., & Ruzzene, M. (2012). Vibration control of plates through hybrid configurations of periodic piezoelectric shunts. *International Journal of Solids and Structures*, 23, 1169.

[19] Celli, P. & Gonella, S. (2014). Low-frequency spatial wave manipulation via phononic crystals with relaxed cell symmetry. *Journal of Applied Physics*, 115(10), 103502.

[20] Celli, P. & Gonella, S. (2015). Manipulating waves with lego® bricks: A versatile experimental platform for metamaterial architectures. *Applied Physics Letters*, 107(8), 081901.

[21] Chen, B. G.-g., Upadhyaya, N., & Vitelli, V. (2014). Nonlinear conduction via solitons in a topological mechanical insulator. *Proceedings of the National Academy of Sciences*, 111(36), 13004–13009.

[22] Chen, L.-S., Kuo, C.-H., & Ye, Z. (2004). Acoustic imaging and collimating by slabs of sonic crystalsmade from arrays of rigid cylinders in air. *Applied Physics Letters*, 85(6), 1072–1074.

[23] Chern, G.-W., Reichhardt, C., & Olson Reichhardt, C. J. (2013). Frustrated colloidal ordering and fully packed loops in arrays of optical traps. *Physical Review E*, 87, 062305.

[24] Chesnais, C., Boutin, C., & Hans, S. (2012). Effects of the local resonance on the wave propagation in periodic frame structures: Generalized newtonian mechanics. *The Journal of the Acoustical Society of America*, 132(4), 2873–2886.

[25] Chong, Y., Wen, X.-G., & Soljačić, M. (2008). Effective theory of quadratic degeneracies. *Physical Review B*, 77(23), 235125.

[26] Christensen, J., Fernandez-Dominguez, A. I., de Leon-Perez, F., Martin-Moreno, L., & Garcia-Vidal, F. J. (2007). Collimation of sound assisted by acoustic surface waves. *Nature Physics*, 3(12), 851–852.

[27] Colquitt, D. J., Jones, I. S., Movchan, N. V., & Movchan, A. B. (2011). Dispersion and localization of elastic waves in materials with microstructure. *Proceedings of the Royal Society of London A: Mathematical, Physical and Engineering Sciences*, 467(2134), 2874–2895.

[28] Daunheimer, S. A., Petrova, O., Tchernyshyov, O., & Cumings, J. (2011). Reducing disorder in artificial kagome ice. *Physical Review Letters*, 107, 167201.

[29] Davis, B. L. & Hussein, M. I. (2014). Nanophononic metamaterial: Thermal conductivity reduction by local resonance. *Physical Review Letters*, 112, 055505.

[30] Ding, Y., Liu, Z., Qiu, C., & Shi, J. (2007). Metamaterial with simultaneously negative bulk modulus and mass density. *Physical Review Letters*, 99, 093904.

[31] Elser, D., Andersen, U. L., Korn, A., Glöckl, O., Lorenz, S., Marquardt, C., & Leuchs, G. (2006). Reduction of guided acoustic wave brillouin scattering in photonic crystal fibers. *Physical Review Letters*, 97, 133901.

[32] Fang, N., Xi, D., Xu, J., Ambati, M., Srituravanich, W., Sun, C., & Zhang, X. (2006). Ultrasonic metamaterials with negative modulus. *Nature Materials*, 5(6), 452–456.

[33] Farhan, A., Derlet, P., Kleibert, A., Balan, A., Chopdekar, R., Wyss, M., Anghinolfi, L., Nolting, F., & Heyderman, L. (2013). Exploring hyper-cubic energy landscapes in thermally active finite artificial spin-ice systems. *Nature Physics*, 9(6), 375–382.

[34] Fleury, R., Sounas, D. L., Sieck, C. F., Haberman, M. R., & Alù, A. (2014). Sound isolation and giant linear nonreciprocity in a compact acoustic circulator. *Science*, 343(6170), 516–519.

[35] Fukui, T., Hatsugai, Y., & Suzuki, H. (2005). Chern numbers in discretized brillouin zone: Efficient method of computing (spin) hall conductances. *Journal of the Physical Society of Japan*, 74(6), 1674–1677.

[36] Giessen, E. v. d. (2011). Materials physics: Bending maxwell's rule. *Nature Physics*, 7, 923–924.

[37] Goldstein, H., Poole, C., & Safko, J. (2002). *Classical Mechanics*. Addison-Wesley San Francisco.

[38] Gonella, S., To, A. C., & Liu, W. K. (2009). Interplay between phononic bandgaps and piezoelectric microstructures for energy harvesting. *Journal of the Mechanics and Physics of Solids*, 57(3), 621–633.

[39] Haldane, F. D. M. (1988). Model for a quantum hall effect without landau levels: Condensed-matter realization of the "parity anomaly". *Physical Review Letters*, 61, 2015–2018.

[40] Haldane, F. D. M. & Raghu, S. (2008). Possible realization of directional optical waveguides in photonic crystals with broken time-reversal symmetry. *Physical Review Letters*, 100, 013904.

[41] Han, Y., Shokef, Y., Alsayed, A. M., Yunker, P., Lubensky, T. C., & Yodh, A. G. (2008). Geometric frustration in buckled colloidal monolayers. *Nature*, 456(7224), 898–903.

[42] Harris, M. J., Bramwell, S. T., McMorrow, D. F., Zeiske, T., & Godfrey, K. W. (1997). Geometrical frustration in the ferromagnetic pyrochlore $ho_2ti_2O_7$. *Physical Review Letters*, 79, 2554–2557.

[43] Hasan, M. Z. & Kane, C. L. (2010). *Colloquium* : Topological insulators. *Reviews of Modern Physics*, 82, 3045–3067.

[44] Hu, X., Chan, C. T., & Zi, J. (2005). Two-dimensional sonic crystals with helmholtz resonators. *Physical Review E*, 71, 055601.

[45] Huang, X., Lai, Y., Hang, Z. H., Zheng, H., & Chan, C. (2011). Dirac cones induced by accidental degeneracy in photonic crystals and zero-refractive-index materials. *Nature Materials*, 10(8), 582–586.

[46] Hussein, M. I., Leamy, M. J., & Ruzzene, M. (2014). Dynamics of phononic materials and structures: Historical origins, recent progress, and future outlook. *Applied Mechanics Reviews*, 66(4), 040802.

[47] Hutchinson, R. & Fleck, N. (2006). The structural performance of the periodic truss. *Journal of the Mechanics and Physics of Solids*, 54(4), 756–782.

[48] Joannopoulos, J. D., Johnson, S. G., Winn, J. N., & Meade, R. D. (2008). *Photonic Crystals: Molding the Flow of Light (Second Edition)*. Princeton University Press, 2 edition.

[49] Kafesaki, M., Sigalas, M. M., & Garcia, N. (2000). Frequency modulation in the transmittivity of wave guides in elastic-wave band-gap materials. *Physical Review Letters*, 85, 4044–4047.

[50] Kane, C. & Lubensky, T. (2014). Topological boundary modes in isostatic lattices. *Nature Physics*, 10(1), 39–45.

[51] Kang, S. H., Shan, S., Košmrlj, A., Noorduin, W. L., Shian, S., Weaver, J. C., Clarke, D. R., & Bertoldi, K. (2014). Complex ordered patterns in mechanical instability induced geometrically frustrated triangular cellular structures. *Physical Review Letters*, 112, 098701.

[52] Khelif, A., Choujaa, A., Benchabane, S., Djafari-Rouhani, B., & Laude, V. (2004). Guiding and bending of acoustic waves in highly confined phononic crystal waveguides. *Applied Physics Letters*, 84(22), 4400–4402.

[53] Kim, E. & Yang, J. (2014). Wave propagation in single column woodpile phononic crystals: Formation of tunable band gaps. *Journal of the Mechanics and Physics of Solids*, 71(0), 33 – 45.

[54] Krödel, S., Thomé, N., & Daraio, C. (2015). Wide band-gap seismic metastructures. *Extreme Mechanics Letters*.

[55] Kushwaha, M. S. (1997). Stop-bands for periodic metallic rods: Sculptures that can filter the noise. *Applied Physics Letters*, 70(24), 3218–3220.

[56] Kushwaha, M. S., Halevi, P., Dobrzynski, L., & Djafari-Rouhani, B. (1993). Acoustic band structure of periodic elastic composites. *Physical Review Letters*, 71, 2022–2025.

[57] Lai, Y., Wu, Y., Sheng, P., & Zhang, Z. (2011). Hybrid elastic solids. *Nature Materials*, 10, 620.

[58] Lammert, P. E., Ke, X., Li, J., Nisoli, C., Garand, D. M., Crespi, V. H., & Schiffer, P. (2010). Direct entropy determination and application to artificial spin ice. *Nature Physics*, 6(10), 786–789.

[59] Langley, R., Bardell, N., & Ruivo, H. (1997). The response of two-dimensional periodic structures to harmonic point loading: a theoretical and experimental study of a beam grillage. *Journal of Sound and Vibration*, 207(4), 521–535.

[60] Li, J., Fok, L., Yin, X., Bartal, G., & Zhang, X. (2009). Experimental demonstration of an acoustic magnifying hyperlens. *Nature Materials*, 8(12), 931–934.

[61] Li, Y., Wu, Y., & Mei, J. (2014). Double dirac cones in phononic crystals. *Applied Physics Letters*, 105(1), –.

[62] Liu, A. J. & Nagel, S. R. (2010). The jamming transition and the marginally jammed solid. *Annual Review of Condensed Matter Physics*, 1(1), 347–369.

[63] Liu, F., Cai, F., Peng, S., Hao, R., Ke, M., & Liu, Z. (2009). Parallel acoustic near-field microscope: A steel slab with a periodic array of slits. *Physical Review E*, 80, 026603.

[64] Liu, F., Huang, X., & Chan, C. (2012a). Dirac cones at k= 0 in acoustic crystals and zero refractive index acoustic materials. *Applied Physics Letters*, 100(7), 071911.

[65] Liu, L. & Hussein, M. I. (2012). Wave motion in periodic flexural beams and characterization of the transition between bragg scattering and local resonance. *Journal of Applied Mechanics*, 79(1), 011003.

[66] Liu, W., Chen, J.-W., & Su, X.-Y. (2012b). Local resonance phononic band gaps in modified two-dimensional lattice materials. *Acta Mechanica Sinica*, 28(3), 659–669.

[67] Liu, Z., Chan, C., & Sheng, P. (2002). Three-component elastic wave band-gap material. *Physical Review B*, 65(16), 165116.

[68] Liu, Z., Zhang, X., Mao, Y., Zhu, Y., Yang, Z., Chan, C., & Sheng, P. (2000). Locally resonant sonic materials. *Science*, 289(5485), 1734–1736.

[69] Lu, L., Joannopoulos, J. D., & Soljačić, M. (2015). Topological photonics. *Nature Photonics*, 8, 821.

[70] Maldovan, M. (2013). Narrow low frequency spectrum and heat management by thermocrystals. *Physical Review Letters*, 110, 025902.

[71] Maldovan, M. & Thomas, E. (2009). *Periodic Materials and Interference Lithography for Photonics, Phononics and Mechanics*. Wiley-VCH.

[72] Mao, X., Xu, N., & Lubensky, T. C. (2010). Soft modes and elasticity of nearly isostatic lattices: Randomness and dissipation. *Physical Review Letters*, 104, 085504.

[73] Martinezsala, R., Sancho, J., Sánchez, J., Gómez, V., Llinares, J., & Meseguer, F. (1995). Sound-attenuation by sculpture. *Nature*, 378(6554), 241–241.

[74] Martinsson, P. & Movchan, A. (2003). Vibrations of lattice structures and phononic band gaps. *The Quarterly Journal of Mechanics and Applied Mathematics*, 56(1), 45–64.

[75] Maxwell, J. C. (1864). L. on the calculation of the equilibrium and stiffness of frames. *Philosophical Magazine Series 4*, 27(182), 294–299.

[76] Mead, D. (1996). Wave propagation in continuous periodic structures: research contributions from southampton, 1964–1995. *Journal of Sound and Vibration*, 190(3), 495–524.

[77] Mei, J., Ma, G., Yang, M., Yang, Z., Wen, W., & Sheng, P. (2012a). Dark acoustic metamaterials as super absorbers for low-frequency sound. *Nature Communications*, 3, 756.

[78] Mei, J., Wu, Y., Chan, C., & Zhang, Z.-Q. (2012b). First-principles study of dirac and dirac-like cones in phononic and photonic crystals. *Physical Review B*, 86(3), 035141.

[79] Mellado, P., Concha, A., & Mahadevan, L. (2012). Macroscopic magnetic frustration. *Physical Review Letters*, 109, 257203.

[80] Milton, G. W. & Willis, J. R. (2007). On modifications of newton's second law and linear continuum elastodynamics. *Proceedings of the Royal Society of London A: Mathematical, Physical and Engineering Sciences*, 463(2079), 855–880.

[81] Moessner, R. & Ramirez, A. P. (2006). Geometrical frustration. *Physics Today*, 59(2), 24.

[82] Molerón, M. & Daraio, C. (2015). Acoustic metamaterial for subwavelength edge detection. *Nature Communications*, 6.

[83] Morgan, J. P., Stein, A., Langridge, S., & Marrows, C. H. (2011). Thermal ground-state ordering and elementary excitations in artificial magnetic square ice. *Nature Physics*, 7(1), 75–79.

[84] Morse, P. M. & Ingard, K. U. (1968). *Theoretical acoustics*. Princeton university press.

[85] Nash, L. M., Kleckner, D., Read, A., Vitelli, V., Turner, A. M., & Irvine, W. T. (2015). Topological mechanics of gyroscopic metamaterials. *arXiv*, (pp. arXiv:1504.03362).

[86] Ni, X., He, C., Sun, X.-C., ping Liu, X., Lu, M.-H., Feng, L., & Chen, Y.-F. (2015). Topologically protected one-way edge mode in networks of acoustic resonators with circulating air flow. *New Journal of Physics*, 17(5), 053016.

[87] O'Hern, C. S., Silbert, L. E., Liu, A. J., & Nagel, S. R. (2003). Jamming at zero temperature and zero applied stress: The epitome of disorder. *Physical Review E*, 68, 011306.

[88] Otsuka, P. H., Nanri, K., Matsuda, O., Tomoda, M., Profunser, D., Veres, I., Danworaphong, S., Khelif, A., Benchabane, S., Laude, V., et al. (2013). Broadband evolution of phononic-crystal-waveguide eigenstates in real-and k-spaces. *Scientific reports*, 3, 3351.

[89] Pauling, L. (1935). The structure and entropy of ice and of other crystals with some randomness of atomic arrangement. *Journal of the American Chemical Society*, 57(12), 2680–2684.

[90] Paulose, J., Chen, B. G.-g., & Vitelli, V. (2015). Topological modes bound to dislocations in mechanical metamaterials. *Nature Physics*, 11, 153.

[91] Pennec, Y., Djafari-Rouhani, B., Vasseur, J. O., Khelif, A., & Deymier, P. A. (2004). Tunable filtering and demultiplexing in phononic crystals with hollow cylinders. *Physical Review E*, 69, 046608.

[92] Phani, A. S. & Fleck, N. A. (2008). Elastic boundary layers in two-dimensional isotropic lattices. *J. Appl. Mech.*, 75(2), 021020.

[93] Phani, A. S., Woodhouse, J., & Fleck, N. (2006). Wave propagation in two-dimensional periodic lattices. *The Journal of the Acoustical Society of America*, 119, 1995.

[94] Picu, R. C. (2011). Mechanics of random fiber networks-a review. *Soft Matter*, 7, 6768–6785.

[95] Prodan, E. & Prodan, C. (2009). Topological phonon modes and their role in dynamic instability of microtubules. *Physical Review Letters*, 103, 248101.

[96] Qi, X.-L. & Zhang, S.-C. (2011). Topological insulators and superconductors. *Reviews of Modern Physics*, 83, 1057–1110.

[97] Qi, Y., Brintlinger, T., & Cumings, J. (2008). Direct observation of the ice rule in an artificial kagome spin ice. *Physical Review B*, 77, 094418.

[98] Raghavan, L. & Phani, A. S. (2013). Local resonance bandgaps in periodic media: Theory and experiment. *The Journal of the Acoustical Society of America*, 134(3), 1950–1959.

[99] Rayleigh, J. W. S. (1896). *The Theory of Sound*, volume 1. Macmillan.

[100] Robertson, W. & Rudy III, J. (1998). Measurement of acoustic stop bands in two-dimensional periodic scattering arrays. *The Journal of the Acoustical Society of America*, 104(2), 694–699.

[101] Ruzzene, M., Scarpa, F., & Soranna, F. (2003). Wave beaming effects in two-dimensional cellular structures. *Smart Materials and Structures*, 12(3), 363.

[102] Sadoc, J.-F. & Mosseri, R. (2006). *Geometrical frustration*. Cambridge University Press.

[103] Sánchez-Dehesa, J., Garcia-Chocano, V. M., Torrent, D., Cervera, F., Cabrera, S., & Simon, F. (2011). Noise control by sonic crystal barriers made of recycled materials. *The Journal of the Acoustical Society of America*, 129(3), 1173–1183.

[104] Sánchez-Pérez, J., Caballero, D., Martinez-Sala, R., Rubio, C., Sánchez-Dehesa, J., Meseguer, F., Llinares, J., & Gálvez, F. (1998). Sound attenuation by a two-dimensional array of rigid cylinders. *Physical Review Letters*, 80(24), 5325.

[105] Shokef, Y., Han, Y., Souslov, A., Yodh, A., & Lubensky, T. C. (2013). Buckled colloidal monolayers connect geometric frustration in soft and hard matter. *Soft Matter*, 9(29), 6565–6570.

[106] Shokef, Y. & Lubensky, T. C. (2009). Stripes, zigzags, and slow dynamics in buckled hard spheres. *Physical Review Letters*, 102, 048303.

[107] Sigalas, M. & Economou, E. (1993). Band structure of elastic waves in two dimensional systems. *Solid State Communications*, 86(3), 141 – 143.

[108] Sigalas, M. & Economou, E. (1996). Attenuation of multiple-scattered sound. *Europhysics Letters*, 36(4), 241.

[109] Skirlo, S. A., Lu, L., Igarashi, Y., Joannopoulos, J., & Soljacic, M. (2015). Experimental observation of large chern numbers in photonic crystals. *arXiv preprint arXiv:1504.04399*.

[110] Skirlo, S. A., Lu, L., & Soljačić, M. (2014). Multimode one-way waveguides of large chern numbers. *Physical Review Letters*, 113(11), 113904.

[111] Spadoni, A., Ruzzene, M., Gonella, S., & Scarpa, F. (2009). Phononic properties of hexagonal chiral lattices. *Wave Motion*, 46(7), 435–450.

[112] Sugimoto, N. & Horioka, T. (1995). Dispersion characteristics of sound waves in a tunnel with an array of helmholtz resonators. *The Journal of the Acoustical Society of America*, 97(3), 1446–1459.

[113] Sun, J.-H. & Wu, T.-T. (2005). Analyses of mode coupling in joined parallel phononic crystal waveguides. *Physical Review B*, 71, 174303.

[114] Sun, K., Souslov, A., Mao, X., & Lubensky, T. (2012). Surface phonons, elastic response, and conformal invariance in twisted kagome lattices. *Proceedings of the National Academy of Sciences*, 109(31), 12369–12374.

[115] Süsstrunk, R. & Huber, S. D. (2015). Observation of phononic helical edge states in a mechanical topological insulator. *Science*, 349(6243), 47–50.

[116] Torrent, D., Mayou, D., & Sánchez-Dehesa, J. (2013). Elastic analog of graphene: Dirac cones and edge states for flexural waves in thin plates. *Physical Review B*, 87, 115143.

[117] Torrent, D. & Sánchez-Dehesa, J. (2012). Acoustic analogue of graphene: Observation of dirac cones in acoustic surface waves. *Physical Review Letters*, 108, 174301.

[118] Torres, M., Montero de Espinosa, F. R., Garcia-Pablos, D., & Garcia, N. (1999). Sonic band gaps in finite elastic media: Surface states and localization phenomena in linear and point defects. *Physical Review Letters*, 82, 3054–3057.

[119] Vasseur, J. O., Hennion, A., Rouhani, B., Duval, F., Dubus, B., & Pennec, Y. (2007). Waveguiding in two-dimensional piezoelectric phononic crystal plates. *Journal of Applied Physics*, 101, 114904.

[120] Vitelli, V. (2012). Topological soft matter: Kagome lattices with a twist. *Proceedings of the National Academy of Sciences*, 109(31), 12266–12267.

[121] von Klitzing, K. (1986). The quantized hall effect. *Reviews of Modern Physics*, 58, 519–531.

[122] Wang, G., Wen, X., Wen, J., Shao, L., & Liu, Y. (2004). Two-dimensional locally resonant phononic crystals with binary structures. *Physical Review Letters*, 93(15), 154302.

[123] Wang, P. & Bertoldi, K. (2014). Towards phononic topological insulators. Presented at APS March Meeting, A42.11.

[124] Wang, P., Casadei, F., Kang, S. H., & Bertoldi, K. (2015a). Locally resonant band gaps in periodic beam lattices by tuning connectivity. *Physical Review B*, 91, 020103.

[125] Wang, P., Casadei, F., Shan, S., Weaver, J. C., & Bertoldi, K. (2014). Harnessing buckling to design tunable locally resonant acoustic metamaterials. *Physical Review Letters*, 113, 014301.

[126] Wang, P., Lu, L., & Bertoldi, K. (2015b). Topological phononic crystals with one-way elastic edge waves. *Physical Review Letters*, 115, 104302.

[127] Wang, P., Shim, J., & Bertoldi, K. (2013a). Effects of geometric and material non-linearities on the tunable response of phononic crystals. *Physical Review B*, 88, 014304.

[128] Wang, R., Nisoli, C., Freitas, R., Li, J., McConville, W., Cooley, B., Lund, M., Samarth, N., Leighton, C., Crespi, V., et al. (2006). Artificial ¡®spin ice¡¯in a geometrically frustrated lattice of nanoscale ferromagnetic islands. *Nature*, 439(7074), 303–306.

[129] Wang, Y.-T., Luan, P.-G., & Zhang, S. (2015c). Coriolis force induced topological order for classical mechanical vibrations. *New Journal of Physics*, 17(7), 073031.

[130] Wang, Z., Chong, Y., Joannopoulos, J., & Soljačić, M. (2009). Observation of unidirectional backscattering-immune topological electromagnetic states. *Nature*, 461(7265), 772–775.

[131] Wang, Z., Chong, Y., Joannopoulos, J. D., & Soljačić, M. (2008). Reflection-free one-way edge modes in a gyromagnetic photonic crystal. *Physical Review Letters*, 100(1), 013905.

[132] Wang, Z., Zhang, P., & Zhang, Y. (2013b). Locally resonant band gaps in flexural vibrations of a timoshenko beam with periodically attached multioscillators. *Mathematical Problems in Engineering*, 2013.

[133] Ward, G. P., Lovelock, R. K., Murray, A. R. J., Hibbins, A. P., Sambles, J. R., & Smith, J. D. (2015). Boundary-layer effects on acoustic transmission through narrow slit cavities. *Physical Review Letters*, 115, 044302.

[134] Wensley, B. G., Batey, S., Bone, F. A., Chan, Z. M., Tumelty, N. R., Steward, A., Kwa, L. G., Borgia, A., & Clarke, J. (2010). Experimental evidence for a frustrated energy landscape in a three-helix-bundle protein family. *Nature*, 463(7281), 685–688.

[135] Wu, Y., Lai, Y., & Zhang, Z.-Q. (2007). Effective medium theory for elastic metamaterials in two dimensions. *Physical Review B*, 76, 205313.

[136] Wyart, M. (2005). On the rigidity of amorphous solids. *Annales de Physique*, 30(3), 1–96.

[137] Xiao, M., Ma, G., Yang, Z., Sheng, P., Zhang, Z., & Chan, C. (2015). Geometric phase and band inversion in periodic acoustic systems. *Nature Physics*, 11(240), 47–50.

[138] Xiao, Y., Wen, J., & Wen, X. (2012). Broadband locally resonant beams containing multiple periodic arrays of attached resonators. *Physics Letters A*, 376(16), 1384–1390.

[139] Yang, S., Page, J. H., Liu, Z., Cowan, M. L., Chan, C. T., & Sheng, P. (2002). Ultrasound tunneling through 3d phononic crystals. *Physical Review Letters*, 88, 104301.

[140] Yang, Z., Gao, F., Shi, X., Lin, X., Gao, Z., Chong, Y., & Zhang, B. (2015). Topological acoustics. *Physical Review Letters*, 114, 114301.

[141] Yilmaz, C., Hulbert, G., & Kikuchi, N. (2007). Phononic band gaps induced by inertial amplification in periodic media. *Physical Review B*, 76(5), 054309.

[142] Yu, D., Liu, Y., Wang, G., Zhao, H., & Qiu, J. (2006a). Flexural vibration band gaps in timoshenko beams with locally resonant structures. *Journal of Applied Physics*, 100(12), 124901.

[143] Yu, D., Liu, Y., Zhao, H., Wang, G., & Qiu, J. (2006b). Flexural vibration band gaps in euler-bernoulli beams with locally resonant structures with two degrees of freedom. *Physical Review B*, 73, 064301.

[144] Yunker, P., Zhang, Z., & Yodh, A. G. (2010). Observation of the disorder-induced crystal-to-glass transition. *Physical Review Letters*, 104, 015701.

[145] Zeng, X., Kieffer, R., Glettner, B., Nürnberger, C., Liu, F., Pelz, K., Prehm, M., Baumeister, U., Hahn, H., Lang, H., et al. (2011). Complex multicolor tilings and critical phenomena in tetraphilic liquid crystals. *Science*, 331(6022), 1302–1306.

[146] Zhang, L., Ren, J., Wang, J.-S., & Li, B. (2010). Topological nature of the phonon hall effect. *Physical Review Letters*, 105, 225901.

[147] Zhang, S., Gilbert, I., Nisoli, C., Chern, G.-W., Erickson, M. J., O¡¯Brien, L., Leighton, C., Lammert, P. E., Crespi, V. H., & Schiffer, P. (2013). Crystallites of magnetic charges in artificial spin ice. *Nature*, 500(7464), 553–557.

[148] Zhang, X. & Liu, Z. (2004). Negative refraction of acoustic waves in two-dimensional phononic ctystals. *Applied Physics Letters*, 85, 341.

[149] Zhu, J., Christensen, J., Jung, J., Martin-Moreno, L., Yin, X., Fok, L., Zhang, X., & Garcia-Vidal, F. (2011). A holey-structured metamaterial for acoustic deep-subwavelength imaging. *Nature physics*, 7(1), 52–55.

This thesis was typeset using LaTeX, originally developed by Leslie Lamport and based on Donald Knuth's TeX. The body text is set in 11 point Egenolff-Berner Garamond, a revival of Claude Garamont's humanist typeface. A template that can be used to format a PhD thesis with this look and feel has been released under the permissive MIT (XII) license, and can be found online at github.com/suchow/Dissertate or from its author, Jordan Suchow, at suchow@post.harvard.edu.